Geochemistry, Geophysics, Geosystems®

AGU ADVANCING EARTH AND SPACE SCIENCE

RESEARCH ARTICLE
10.1029/2022GC010470

# Ocean-Forced Instability of the West Antarctic Ice Sheet Since the Mid-Pleistocene

**Jiakai Wang[1,2], Zheng Tang[3,4], David J. Wilson[5], Fengming Chang[1,2,4], Zhifang Xiong[3,4], Dongyong Li[6], and Tiegang Li[2,3,4]**

[1]Key Laboratory of Marine Geology and Environment, Institute of Oceanology, Chinese Academy of Sciences, Qingdao, China, [2]University of Chinese Academy of Sciences, Beijing, China, [3]Key Laboratory of Marine Geology and Metallogeny, First Institute of Oceanography, Ministry of Natural Resources, Qingdao, China, [4]Laboratory for Marine Geology, Qingdao National Laboratory for Marine Science and Technology, Qingdao, China, [5]Institute of Earth and Planetary Sciences, University College London and Birkbeck, University of London, London, UK, [6]Key Laboratory of Submarine Science and Prospecting Technology, Ministry of Education, Ocean University of China, Qingdao, China

**Key Points:**

- Interglacial ocean-forced instability of the West Antarctic Ice Sheet (WAIS) has existed since at least ~770 ka
- Differences in sediment provenance before and after Marine Isotope Stage (MIS) 16 may relate to different states of high-latitude atmospheric and ocean circulation
- Strong ocean and orbital forcing may have enhanced WAIS instability from MIS 13 to MIS 15

**Supporting Information:**

Supporting Information may be found in the online version of this article.

**Correspondence to:**

T. Li,
tgli@fio.org.cn

**Citation:**

Wang, J., Tang, Z., Wilson, D. J., Chang, F., Xiong, Z., Li, D., & Li, T. (2022). Ocean-forced instability of the West Antarctic Ice Sheet since the Mid-Pleistocene. *Geochemistry, Geophysics, Geosystems*, *23*, e2022GC010470. https://doi.org/10.1029/2022GC010470

Received 6 APR 2022
Accepted 29 JUL 2022

**Author Contributions:**

**Conceptualization:** Jiakai Wang, Tiegang Li
**Data curation:** Jiakai Wang
**Formal analysis:** Jiakai Wang, David J. Wilson, Fengming Chang
**Funding acquisition:** Zheng Tang, Fengming Chang, Zhifang Xiong, Tiegang Li
**Investigation:** Jiakai Wang, Zheng Tang
**Methodology:** Jiakai Wang, Dongyong Li
**Project Administration:** Zhifang Xiong, Tiegang Li
**Resources:** Zheng Tang, Zhifang Xiong, Tiegang Li



**Abstract** Evidence on West Antarctic Ice Sheet (WAIS) instability through Pleistocene glacial/interglacial cycles can provide fundamental constraints on interactions between the climate system and cryosphere. To explore such ice sheet-ocean-climate processes on orbital timescales over the last ~770 ka, we provide continuous records of iceberg-rafted debris (IRD) content and clay mineralogy, supported by detrital Sr-Nd isotopes from the pronounced IRD peaks, in gravity core ANT34/A2-10 from the Amundsen abyssal plain. The IRD record reveals interglacial WAIS instability since ~770 ka, while comparison to the clay mineralogy record and published records of regional oceanic and atmospheric forcing suggests a temporal link with a strengthened Antarctic Circumpolar Current, enhanced deepwater ventilation, and poleward-shifted southern westerly winds. In addition, the Sr-Nd isotope signature of the detrital sediments indicates a shift in provenance around Marine Isotope Stage (MIS) 16, potentially linked to regional oceanic circulation changes. We suggest that an expanded Ross Gyre was important for controlling iceberg trajectories and sediment transport to the site before MIS 16, whereas modern-like iceberg trajectories were established after MIS 16, probably related to a poleward shift of the Amundsen Sea Low after the end of the Mid-Pleistocene Transition. This reorganization of the ocean and atmospheric circulation was followed by an interval of enhanced WAIS variability during MIS 15 to 13, which was linked to strong orbital and ocean forcing. These insights into the role of ocean-atmosphere forcing on the past behavior of the WAIS may improve our framework for understanding future changes in this region.

**Plain Language Summary** Understanding the vulnerability of the West Antarctic Ice Sheet (WAIS) to a warming climate is critical for constraining its future contributions to global sea-level rise. Previous studies on marine sediment cores have provided evidence for WAIS instability in response to warming ocean waters during recent glacial/interglacial cycles. Here, we extend such work over a longer timescale by generating iceberg-rafted debris (IRD) content and clay mineralogy records from the Amundsen Sea offshore of West Antarctica back to ~770 ka. Enhanced IRD content during warm interglacial periods provides evidence for the instability of the WAIS and was accompanied by a shift in clay mineralogy. These changes also coincided with a strengthened Antarctic Circumpolar Current, poleward-shifted southern westerly winds, and improved deepwater ventilation, as indicated by existing studies. This comparison supports ocean forcing as a driver of WAIS instability since ~770 ka. We also measured strontium and neodymium isotope signatures on selected samples, revealing a switch in sediment supply around Marine Isotope Stage 16 that was probably related to the reorganization of atmospheric and oceanic circulation. The subsequent interval of strong orbital and ocean forcing led to pronounced WAIS variability from ~480 to 580 ka. These findings improve our framework for understanding future changes in this region.

## 1. Introduction

The cryosphere plays an essential role in the global climate system by influencing sea level, ocean circulation, and the carbon cycle over a range of timescales (Bell, 2008; Golledge et al., 2019; Lear et al., 2004; Lindgren et al., 2018; Wadham et al., 2019). In particular, the Antarctic Ice Sheet represents the largest potential contributor to future global sea-level rise (Nerem et al., 2018; Shepherd, Ivins, et al., 2018; Tinto et al., 2019). Increased iceberg calving and basal melting of ice shelves reduce their buttressing effect and accelerate the loss of ice

**Supervision:** Zheng Tang, David J. Wilson, Tiegang Li
**Validation:** Jiakai Wang
**Visualization:** Jiakai Wang
**Writing – original draft:** Jiakai Wang
**Writing – review & editing:** Jiakai Wang, David J. Wilson, Fengming Chang, Tiegang Li

from upstream of the grounding line, which has led to increased sea-level contributions from Antarctica in recent years (Rignot et al., 2019; Shepherd, Fricker, et al., 2018). The ongoing ice mass loss from the Antarctic Ice Sheet is mainly occurring in the West Antarctic Ice Sheet (WAIS), where the basal melting of floating ice shelves is accelerating the retreat of grounding lines (Pattyn & Morlighem, 2020). This contemporary process has also occurred in the past, as demonstrated by modeling simulations (DeConto & Pollard, 2016; Pollard & DeConto, 2009; Pollard et al., 2015; Sutter et al., 2019) and geological records (Conway et al., 1999; Hillenbrand et al., 2012, 2017; Levy et al., 2019).

The South Pacific sector of the WAIS has margins adjacent to the Ross, Amundsen, and Bellingshausen Seas (Figure 1a). Its ice shelves, including the Ross Ice Shelf, Getz Ice Shelf, and Pine Island Ice Shelf, buttress the rapidly flowing ice streams of the WAIS, restricting their drainage into the Southern Ocean (Davis et al., 2018; Joughin & Alley, 2011; Pritchard et al., 2012). Recent studies suggest that the grounding line in this sector of the WAIS is retreating irreversibly, due to ocean-forced ice mass loss linked to the loss of buttressing ice shelves, and that this process may accelerate future ice loss (Jones et al., 2021; Joughin et al., 2014; Rignot et al., 2013, 2014, 2019; Schmidtko et al., 2014; S. S. Jacobs et al., 2011; Thoma et al., 2008). Iceberg calving from the Antarctic Ice Sheet represents around half of the total ice mass loss in recent decades (Gladstone et al., 2001; Silva et al., 2006), while the ice mass loss from the South Pacific sector of the WAIS is dominated by iceberg calving, with a relatively minor contribution from basal melting (Shepherd, Ivins, et al., 2018; S. S. Jacobs et al., 1992).

In recent decades, the increased upwelling of relatively warm Circumpolar Deep Water (CDW) and/or Modified Circumpolar Deep Water (MCDW) in the South Pacific sector of the Southern Ocean has accelerated the basal melt rate in this sector of the WAIS (Rignot et al., 2013; S. S. Jacobs et al., 1996, 2011; Thoma et al., 2008), especially in the Amundsen and Bellingshausen Seas (Nakayama et al., 2018; Pritchard et al., 2012; Rignot & Jacobs, 2002; S. S. Jacobs et al., 2011; Thoma et al., 2008). Moreover, this ocean-forced destabilization of the WAIS is not only occurring in the present (Rignot et al., 2019; Shepherd, Fricker, et al., 2018; Shepherd, Ivins, et al., 2018; S. S. Jacobs et al., 2011; Wahlin et al., 2021), but has been shown to have occurred during the Holocene (Hillenbrand et al., 2017; Jones et al., 2021; Peck et al., 2015; Totten et al., 2022), the last deglaciation (Lowe & Anderson, 2002; Weber et al., 2014), and in previous interglacials (Turney et al., 2020). However, there are fewer constraints on how this ocean-forced ice-sheet instability mechanism has operated over orbital time scales before the Late Pleistocene (Levy et al., 2019; Pollard & DeConto, 2009; Teitler et al., 2010).

Here, to explore the connections between high-latitude ocean-atmosphere processes and WAIS dynamics on orbital timescales, we present semi-quantitative iceberg-rafted debris (IRD) abundance (wt% and grains/g) and clay mineralogy records from a sediment core in the Pacific sector of the Southern Ocean spanning the last ~770 ka. By comparing these records to published benthic carbon isotope ($\delta^{13}C$) records (Hodell et al., 2003; Ullermann et al., 2016), deep ocean ventilation proxies (Tang et al., 2022), Antarctic Circumpolar Current (ACC) flow-speed reconstructions (Toyos et al., 2020; S. Wu, Lembke-Jene, et al., 2021), and Antarctic ice core data constraining Southern Westerly Wind (SWW) migration (Fudge et al., 2013; R. F. Anderson et al., 2009), we assess the role of ocean forcing in driving destabilization of the WAIS. In addition, we use the combination of clay minerals and Sr-Nd isotope data on bulk detrital sediments and IRD samples to provide constraints on iceberg sourcing and pathways and to investigate changes in the high-latitude coupled atmospheric-oceanic circulation patterns during those peak IRD intervals.

## 2. Regional Setting

Gravity core ANT34/A2-10 was recovered from 125.58°W, 67.03°S at a water depth of 4,217 m by the *R/V Xuelong* during the 34th Chinese National Antarctic Research Expedition in 2018. The core site is located on the Amundsen Abyssal Plain at the northern edge of the Amundsen Sea, adjacent to Marie Byrd Land, in the South Pacific sector of the Southern Ocean (Figure 1). It lies between the Southern Boundary of the Antarctic Circumpolar Current (SBACC) and the Southern Antarctic Circumpolar Current Front (SACCF; Figure 1a), with its bottom waters influenced by Antarctic Bottom Water (AABW; Uenzelmann-Neben & Gohl, 2012) derived mainly from the western Ross Sea (WRS; Gordon et al., 2009; Orsi & Wiederwohl, 2009; Figure 1b). The ACC flows eastward at intermediate and deep depths around Antarctica (Orsi et al., 1995; S. S. Jacobs & Comiso, 1997;

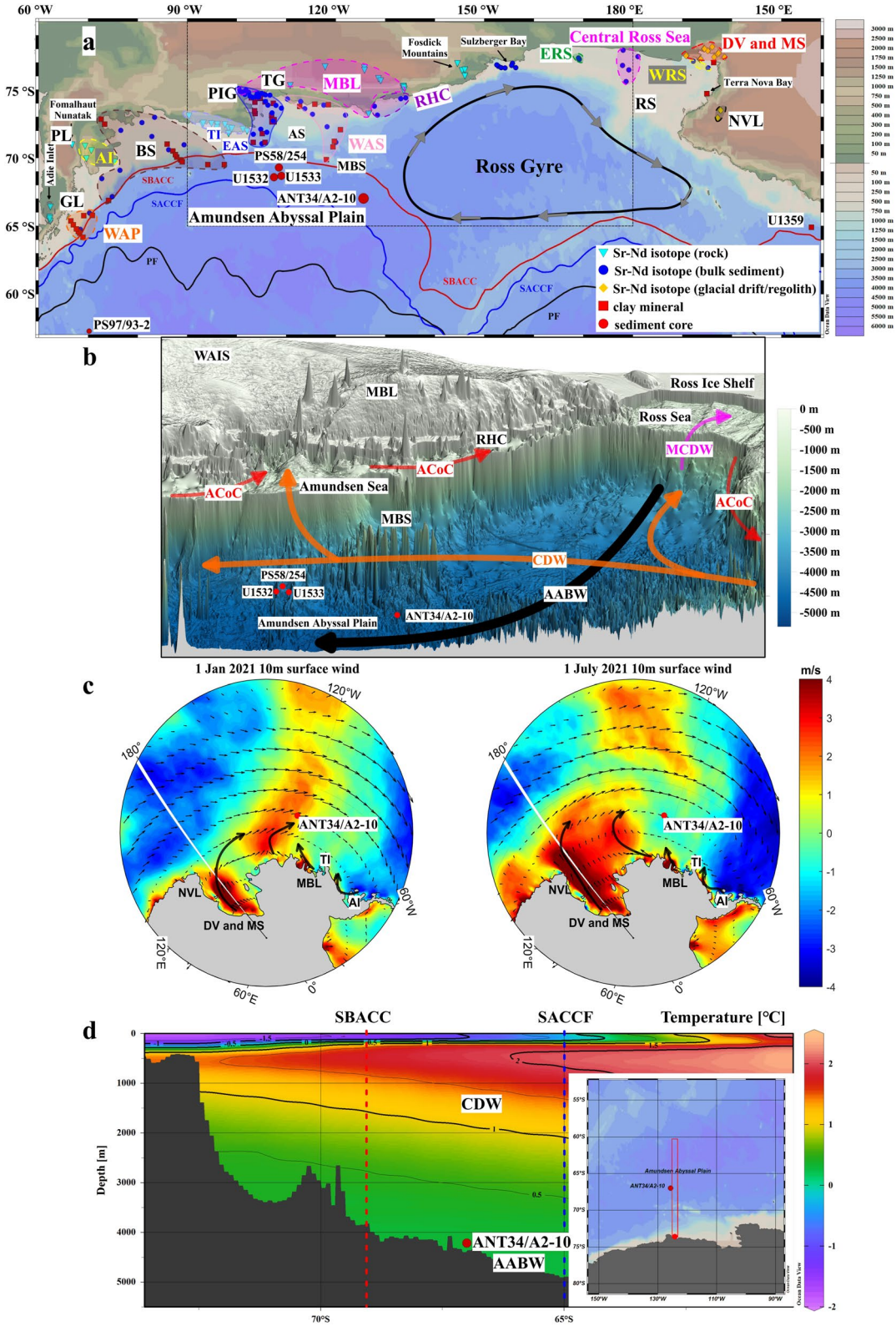
a
60 °W
90 °W
120 °W
150 °W
180 °E
150 °E
75 °S
70 °S
65 °S
60 °S
Fosdick Mountains
Sulzberger Bay
Central Ross Sea
DV and MS
ERS
WRS
Terra Nova Bay
RS
NVL
PIG
TG
MBL
RHC
Fomalhaut Nunatak
PL
AI
BS
TI
EAS
AS
WAS
PS58/254
MBS
Adie Inlet
SBACC
SACCF
U1532
U1533
ANT34/A2-10
Amundsen Abyssal Plain
Ross Gyre
GL
WAP
PF
U1359
PS97/93-2
Sr-Nd isotope (rock)
Sr-Nd isotope (bulk sediment)
Sr-Nd isotope (glacial drift/regolith)
clay mineral
sediment core
b
WAIS
MBL
Ross Ice Shelf
Ross Sea
RHC
MCDW
ACoC
Amundsen Sea
MBS
CDW
AABW
PS58/254
U1532
U1533
Amundsen Abyssal Plain
ANT34/A2-10
0 m
-500 m
-1000 m
-1500 m
-2000 m
-2500 m
-3000 m
-3500 m
-4000 m
-4500 m
-5000 m
c
1 Jan 2021 10m surface wind
1 July 2021 10m surface wind
m/s
120°W
180°
60°W
120°E
60°E
0°
ANT34/A2-10
TI
MBL
NVL
AI
DV and MS
d
SBACC
SACCF
Temperature [°C]
Depth [m]
CDW
AABW
70°S
65°S

**Figure 1.**

S. Jacobs et al., 2012), while the Antarctic Coastal Current in the surface ocean is driven by the easterly winds and flows westward parallel to the Antarctic coastline (Figure 1b).

Most layers of the ACC are occupied by CDW (Orsi et al., 1995; Rickli et al., 2014), a relatively warm, high-salinity water mass that generally circulates along the pathways of the ACC and the Ross Gyre (Orsi et al., 1995; Figure 1b). Some CDW upwells south of the SBACC onto the Ross Sea shelf and other narrower continental shelf areas, where it is ultimately modified by sea-ice formation and feeds into the formation of AABW (Orsi et al., 1999). Moreover, the modification of the incoming CDW near the outer edge of the Ross Sea produces MCDW (Figure 1b), which is warmer (temperatures up to 0.95°C) than surrounding waters and has a salinity that is intermediate between the surface and deep water masses (Orsi & Wiederwohl, 2009). This MCDW is the primary source of heat, salt, and nutrients to the Ross Sea continental shelf region (Budillon & Spezie, 2004; Hiscock, 2004; W. O. Smith et al., 2006). Such local incursions of CDW and MCDW far onto the inner continental shelves toward the WAIS margins in the Amundsen and Ross Seas (Das et al., 2020; S. Jacobs et al., 2012; Figure 1b) make the South Pacific marine-based WAIS highly sensitive to ocean thermal forcing.

## 3. Materials and Methods

### 3.1. Material

Gravity core ANT34/A2-10 is 4.54 m long and was split lengthwise and logged in detail by visual examination. Its lithology is characterized by mainly pelagic silty clay and occasional volcaniclastic material, with a foraminifer-rich layer at 11–29 cm, and frequent occurrence of radiolarians from 0 to 110 cm (Figure 2). The entire core is dominated by silty clay with no significant sedimentary structures, except for thin planar laminations (less than 3 mm thick) at 401–454 cm depth, which may reflect sorted silts or possibly diatom mat deposition (Figure 2). There is no clear evidence of turbidite sedimentation or mass redeposition, with the possible exception of the laminated section from 401 to 454 cm as noted above. Large clasts were found at 234–238, 338–340, and 346–350 cm (Figure 2). The entire core was segmented at 2 cm intervals to analyze IRD content and clay mineralogy, and Sr-Nd isotopic composition was measured on selected bulk detrital samples.

### 3.2. Analytical Methods

Approximately 5–10 g of original wet samples from core ANT34/A2-10 were reacted with 10% acetic acid and 3.5% hydrogen peroxide to remove carbonate and organic matter, respectively, before being dried, weighed, and separated by wet sieving (150 μm) to obtain the operationally defined IRD component (Caniupán et al., 2011). The >150 μm fraction was dried under 55°C, and the 150 μm-2 mm fraction was obtained by dry sieving through a 2 mm mesh. The semi-quantitative IRD weight percentage (IRD wt%) was calculated by dividing the weight of the coarse fraction (150 μm-2 mm) by the dried bulk carbonate- and organic matter-free sample weight (Caniupán et al., 2011; L. Wu, Wilson, et al., 2021). In addition, the number of particles in the 150 μm-2 mm fraction was counted under a binocular microscope (LEICA S8AP0), with subangular to subrounded quartz and feldspar grains and rock fragments considered to represent the main IRD components (Kanfoush et al., 2000; Starr et al., 2021; Teitler et al., 2010; Watkins et al., 1974); these data are reported as the semi-quantitative IRD content (IRD grains/g). Although radiolarian shells with sizes of 150 μm-2 mm frequently appeared in some layers of ANT34/A2-10, their abundance and weights were too low to contribute significantly to the IRD wt% record. Furthermore, the opal content in the bulk sediment was typically ~12% and always less than 20%, so any changes in opal content do not significantly contribute to the downcore patterns in the IRD proxies. We also note

**Figure 1.** Geographic and oceanographic setting of the study area: (a) location map of the relevant core sites and regional sediment sources; (b) three-dimensional topographic map showing the core sites and major ocean currents; (c) modern 10 m sea surface winds in the study area, from selected days in austral summer (left) and winter (right) (vectors indicate wind direction; color shading indicates wind strength); and (d) hydrographic section showing temperature structure of the Amundsen Sea. The ocean fronts in panels (a and d) are from Orsi et al. (1995). The dashed line in panel (a) represents the boundary for panel (b). The wind stress data in panel (c) are from the website (https://coastwatch.pfeg.noaa.gov), and the black arrows represent the approximate wind stress direction. Temperature data in panel (d) are from the World Ocean Atlas 2018 (https://odv.awi.de/en/data/ocean/world-ocean-atlas-2018/). Geographic settings: WAIS, West Antarctic Ice Sheet; NVL, North Victoria Land; DV, Dry Valleys; MS, McMurdo Sound; RHC, Ruppert and Hobbs Coasts; MBL, Marie Byrd Land; GL, Graham Land; PL, Palmer Land; WAP, West Antarctic Peninsula; TI, Thurston Island; AI, Alexander Island; TG, Thwaites Glacier; PIG, Pine Island Glacier; MBS, Marie Byrd Seamount; RS, Ross Sea; AS, Amundsen Sea; BS, Bellingshausen Sea; EAS/WAS, Eastern/Western Amundsen Sea; ERS/WRS, Eastern/Western Ross Sea. Water masses and fronts: AABW, Antarctic Bottom Water; CDW, Circumpolar Deep Water; MCDW, Modified Circumpolar Deep Water; ACoC, Antarctic Coastal Current; PF, Polar Front; SBACC, Southern Boundary of Antarctic Circumpolar Current Front; SACCF, Southern Antarctic Circumpolar Current Front.

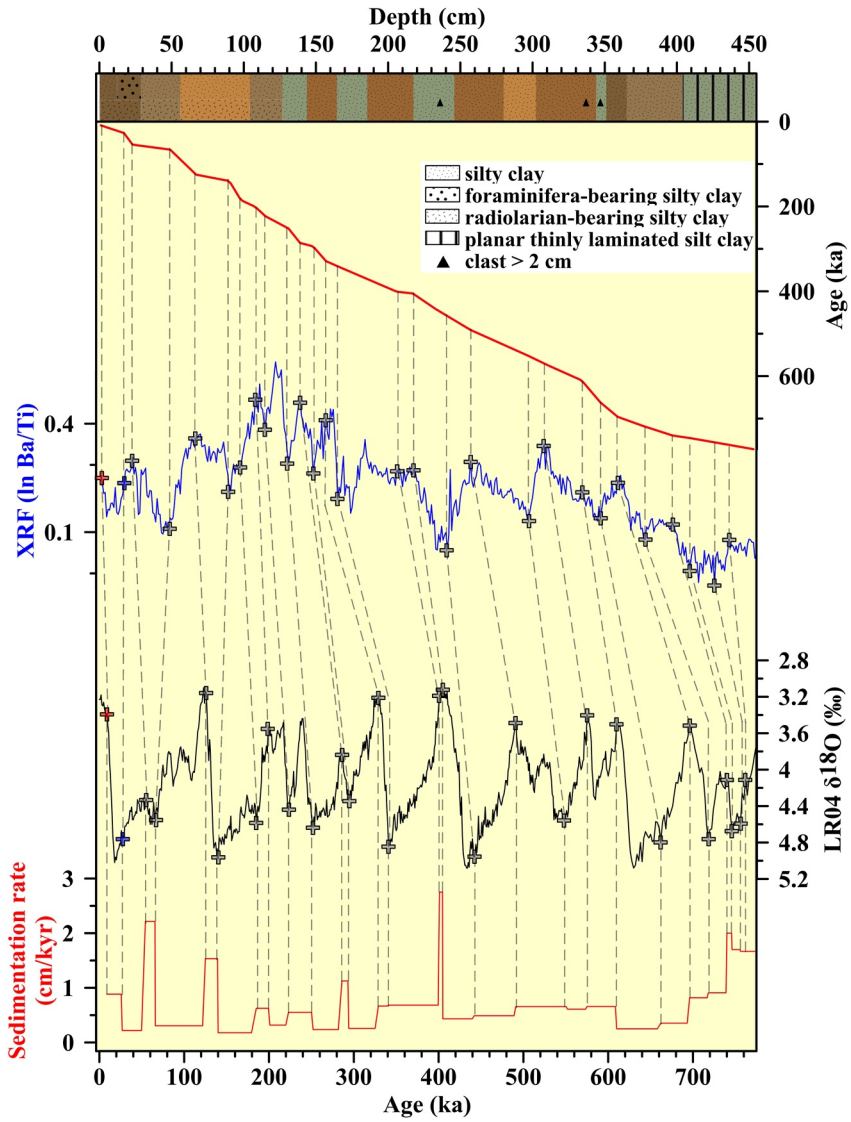


**Figure 2.** Age model and lithological characteristics of core ANT34/A2-10. Panels from top to bottom show sediment log, age-depth model, ln(Ba/Ti) from XRF-scanning (on depth scale), global benthic LR04 $\delta^{18}O$ stack (Lisiecki & Raymo, 2005), and sedimentation rates (on age scale). Vertical gray dashed lines are age-depth tie points from Tang et al. (2022). Gray crosses: tie points based on Ba/Ti. Red cross: organic carbon AMS $^{14}C$ date on bulk acid-insoluble organic carbon. Blue cross: foraminiferal AMS $^{14}C$ date. See Tables S1 and S2 in Supporting Information S1 for further details on the age model.

that volcanic particles and micronodules were not a significant component in most layers of core ANT34/A2-10 and are unlikely to contribute significantly to downcore variations in the IRD proxy records. This point is also supported by the good agreement between the IRD counts, where such components could be manually excluded, and the IRD wt% records.

For clay mineralogy, 227 samples were processed to obtain the <2 μm fraction, with separation based on Stokes' settling velocity principle, after removing carbonate and organic matter by reacting with acetic acid and excess $H_2O_2$ (S. Wan et al., 2010). X-ray diffraction analysis of the samples was performed with a Brucker D8 ADVANCE diffractometer, using oriented mounts and CuKα radiation (40 kV, 40 mA), in the Key Laboratory of Marine Geology and Environment at the Institute of Oceanology, Chinese Academy of Sciences. Each sample was measured two times after ethylene-glycol solvation (i.e., (a) 3°–30° 2$\theta$, 0.02° steps; (b) 24°–26° 2$\theta$, 0.01° steps) to identify the double peak of 3.58/3.54 Å (chlorite/kaolinite) (S. Wan et al., 2006, 2007). Semi-quantitative estimates of the major clay mineral groups (smectite, kaolinite, illite, and chlorite) were based on the integrated peak areas of the

characteristic basal reflections (smectite—17 Å, illite—10 Å, and chlorite/kaolinite—7 Å) in the glycolate state, using Topas 2P software with the experimental factors of (Biscaye, 1965). The relative proportions of chlorite and kaolinite were determined based on the ratio of the 3.58/3.54 Å peak areas (chlorite/kaolinite) in the glycolate state. Relative clay mineral abundances are given in percent, with the analytical precision (relative standard deviation) for the abundance of each clay mineral estimated to be approximately ±5% (S. Wan et al., 2010). The illite chemical index was calculated from the ratio of the 5 and 10 Å illite peak areas (Esquevin Index) in the glycolate state (Esquevin, 1969). Ratios higher than 0.4 represent Al-rich illite formed under strong hydrolysis, whereas ratios lower than 0.4 correspond to Fe-Mg illite, which is a product of physical rock weathering (Ehrmann, 1998; Gingele et al., 2001). The illite and smectite crystallinity were estimated from the full width at half maximum (FWHM) of the illite 10 Å peak and smectite 17 Å peak, respectively. Generally, high FWHM values indicate poor crystallinities, whereas low FWHM values indicate good crystallinities.

Detrital strontium (Sr) and neodymium (Nd) isotopes were analyzed on 11 bulk sediment samples (~100 mg), predominantly taken from IRD peak intervals, and on 3 IRD (>250 μm) samples (~50 to 100 mg) from IRD peak intervals. The samples were processed in the Key Laboratory of Marine Geology and Metallogeny, First Institute of Oceanography, Ministry of Natural and Resources (FIO). First, the samples were ground and leached to remove any authigenic ferromanganese oxide phases using 1 M hydroxylamine hydrochloride/25% buffered acetic acid at 90°C for 3 hr. They were then transferred to Teflon beakers and digested in a mixture of 2 mL HF, 1.5 mL $HNO_3$, and 0.2 mL $HClO_4$ on an electric heating plate at 120°C for about a week until completely dissolved. After evaporation at 180°C, the samples were dissolved in 2.5 M HCl and the supernatant after centrifugation was processed through ion-exchange columns, with Sr separated using AG50W-X12 resin and Nd using LN-B50-A resin.

The Sr and Nd isotopic compositions were analyzed on a NuInstruments Plasma 1 HR multi-collector inductively coupled plasma mass spectrometer (MC-ICP-MS), in the FIO, or on a ThermoScientific Neptune MC-ICP-MS in the Key Laboratory of Submarine Science and Prospecting Technology, Ministry of Education, Ocean University of China (OUC; Table 1). The $^{87}Sr/^{86}Sr$ ratios and $^{143}Nd/^{144}Nd$ ratios were corrected for instrumental mass bias using the exponential law ($^{88}Sr/^{86}Sr = 8.375$ and $^{146}Nd/^{144}Nd = 0.7219$). In the FIO, accuracy was assessed by analyzing reference standards NBS 987 ($^{87}Sr/^{86}Sr = 0.710252 \pm 0.000013$) and Shin Etsu JNdi-1 ($^{143}Nd/^{144}N$

**Table 1**
*Sr and Nd Isotopic Compositions of Bulk Detrital Sediment Samples From Core ANT34/A2-10*

| Sample type | Mid-depth (cm) | IRD peak interval | Age (ka) | $^{143}Nd/^{144}Nd$[a] | SE[b] | $^{87}Sr/^{86}Sr$ | SE[c] | $\varepsilon_{Nd}$ | 2SD[b] |
|---|---|---|---|---|---|---|---|---|---|
| Bulk detrital residue | 11 | MIS 2 | 20 | 0.512457* | 0.000004 | 0.710295 | 0.000005 | −3.52 | 0.16 |
| Bulk detrital residue | 35 | I1 | 60 | 0.512508 | 0.000004 | 0.710617 | 0.000004 | −2.54 | 0.29 |
| Bulk detrital residue | 55 | I2 | 86 | 0.512506 | 0.000006 | 0.710498 | 0.000004 | −2.57 | 0.29 |
| Bulk detrital residue | 61 | I2 | 105 | 0.512466 | 0.000003 | 0.710463 | 0.000005 | −3.36 | 0.29 |
| Bulk detrital residue | 107 | I3 | 200 | 0.512461* | 0.000004 | 0.710267 | 0.000010 | −3.45 | 0.16 |
| Bulk detrital residue | 177 | I5 | 359 | 0.512470 | 0.000007 | 0.710709 | 0.000007 | −3.28 | 0.29 |
| Bulk detrital residue | 219 | I6 | 410 | 0.512438* | 0.000004 | 0.710804 | 0.000006 | −3.90 | 0.17 |
| Bulk detrital residue | 269 | I7 | 509 | 0.512446 | 0.000003 | 0.710390 | 0.000005 | −3.74 | 0.29 |
| Bulk detrital residue | 311 | I8 | 575 | 0.512439 | 0.000005 | 0.710815 | 0.000006 | −3.88 | 0.29 |
| Bulk detrital residue | 389 | I11 | 731 | 0.512401* | 0.000005 | 0.712760 | 0.000007 | −4.63 | 0.19 |
| Bulk detrital residue | 421 | I12 | 753 | 0.512384 | 0.000005 | 0.713400 | 0.000004 | −4.96 | 0.29 |
| >250 μm detrital residue | 261 | I7 | 497 | 0.512700 | 0.000004 | 0.707030 | 0.000007 | 1.21 | 0.29 |
| >250 μm detrital residue | 311 | I8 | 575 | 0.512482 | 0.000006 | 0.711175 | 0.000005 | −3.05 | 0.29 |
| >250 μm detrital residue | 353 | I10 | 679 | 0.512228 | 0.000005 | 0.717786 | 0.000004 | −8.01 | 0.29 |

[a]All Sr and Nd isotope data were measured at the Key Laboratory of Marine Geology and Metallogeny, First Institute of Oceanography, Ministry of Natural Resources, except for the Nd isotope data marked (*) which were measured at the Key Laboratory of Submarine Science and Prospecting Technology, Ministry of Education, Ocean University of China. [b]External reproducibility based on JNdi-1 or GSB 04-3258-2015 standards is 0.000015 (2SD) or 0.000007 (2SD), respectively, for $^{143}Nd/^{144}Nd$. The 2SD on $\varepsilon_{Nd}$ values is based on this external reproducibility unless the internal 2SE is larger. [c]External reproducibility based on NBS 987 standards is 0.000038 (2SD) for $^{87}Sr/^{86}Sr$.

d = 0.512115 ± 0.000007; Tanaka et al., 2000; Weis et al., 2006). The external reproducibility was estimated from the within-session 2$\sigma$ on NBS 987 and JNdi-1 standards, which gave $^{87}Sr/^{86}Sr = 0.710254 \pm 0.000038$ (2$\sigma$, $n = 20$) and $^{143}Nd/^{144}Nd = 0.512114 \pm 0.000015$ (2$\sigma$, $n = 15$). For Nd isotope analyses in the OUC, accuracy was assessed using reference standard GSB 04-3258-2015 ($^{143}Nd/^{144}Nd = 0.512438 \pm 0.000005$; J. Li et al., 2017). The external reproducibility was estimated from the within-session 2$\sigma$ on the GSB 04-3258-2015 standard, which gave $^{143}Nd/^{144}Nd = 0.512438 \pm 0.000007$ (2$\sigma$, $n = 2$). The Nd isotope data of samples are expressed in epsilon notation, $\varepsilon_{Nd} = [(^{143}Nd/^{144}Nd)_{sample}/(^{143}Nd/^{144}Nd)_{CHUR} - 1] \times 10^4$, where CHUR is the Chondritic Uniform Reservoir value (0.512638) (Jacobsen & Wasserburg, 1980). Typical bulk detrital samples yielded 2–3 μg Nd, whereas typical Nd blanks in this laboratory are ~1 pg Nd, so blank contributions are negligible.

### 3.3. Age Model

Previous studies of Pleistocene sediments from the Antarctic margin have developed orbital-scale age models using correlations between surface-water productivity proxies (such as biogenic opal, silica, Ba/Ti ratios, or XRF-scanning Ba/Ti count ratios) and the LR04 benthic $\delta^{18}O$ stack (Ceccaroni et al., 1998; Hillenbrand et al., 2009; Presti et al., 2011; Wu et al., 2017), often in combination with biostratigraphy or magnetostratigraphy. In a recent study (Tang et al., 2022), the age model of core ANT34/A2-10 was established by correlating the XRF-scanning Ba/Ti ratios to the LR04 benthic $\delta^{18}O$ stack (Lisiecki & Raymo, 2005). The age model uses 26 age control points based on comparison of the Ba/Ti ratios to the LR04 $\delta^{18}O$ stack and two AMS $^{14}C$ age control points (planktonic foraminifera and bulk organic carbon) (Figure 2), and was not further modified here. For detailed information on the age model, see Tables S1 and S2 in Supporting Information S1.

According to the age model, core ANT34/A2-10 spans the last ~770 ka, with an average sedimentation rate of 0.59 cm/kyr (Figure 2). In comparison, the average sedimentation rate over this interval in core PS58/254 was 1.8 cm/kyr, and sedimentation rates in the Pleistocene intervals of cores U1532 and U1533 were 2.0 and 1.4 cm/kyr, respectively (Gohl et al., 2021). All of these three cores were collected nearby, at similar depths but closer to the shelf break than our site (Figures 1a and 1b). We note that we are unable to provide biostratigraphic constraints on core ANT34/A2-10, which could lead to some uncertainty in the age model, particularly in its deeper sections or where sub-orbital timescales are considered. Nevertheless, Tang et al. (2022) verified the reliability of this age model based on the consistency between the downcore magnetic susceptibility record of core ANT334/A2-10 and the dust concentration record from the EPICA Dome C (EDC) ice core (Tang et al., 2022). In addition, the similar glacial/interglacial cyclicity of the sedimentary records between core ANT34/A2-10 and core PS58/254 (Hillenbrand et al., 2009; Konfirst et al., 2012) provides further reasonable validation for the reliability of this age model over glacial/interglacial timescales (see Text S1 and Figure S1 in Supporting Information S1).

## 4. Results

### 4.1. Variability in IRD Inputs Through Glacial/Interglacial Cycles

The record of IRD counts (grains/g) is similar to the record of IRD wt% (150 μm-2 mm) (Figure 3a), with $R^2 = 0.72$. Most of the IRD consists of sand-sized quartz and feldspar grains, with only occasional minor amounts of gravel (Figure 2). Both records show higher abundance during interglacial periods than glacial periods, with peak counts of up to ~640 grains/g and ~3.6 wt% (Figure 3a). The highest amplitude variations and largest IRD peaks occurred at ~474 to 530 ka (Marine Isotope Stage [MIS] 13) and ~550 to 580 ka (MIS 15).

The coretop age of ANT34/A2-10 is ~8.8 ka (Table S1 in Supporting Information S1), indicating a hiatus that likely reflects sample loss or disturbance during piston coring. As such, the IRD abundance in the Holocene layer should be taken with some caution and may not provide a good baseline for understanding the past behavior. We therefore identified IRD peak intervals' based on the assumptions that (a) the high IRD content predominantly relates to warm interglacial periods and can be compared to a glacial baseline and (b) the IRD peak intervals should be characterized by a higher IRD content than the average IRD content of glacial periods (i.e., 146 grains/g and 0.74 wt%) (Figures 4a and 4b). Having identified the major orbital-scale IRD peak intervals, labeled as I1 to I12 (Figure 4a), we determined their boundaries by comparison to the glacial average values for the IRD proxies. Nearly all IRD peak intervals occur during interglacial periods, with only two IRD peak intervals appearing to occur during glacial periods; these latter two IRD peaks (I11 and I12) are found near the base of the core during MIS 18, according to the age model.

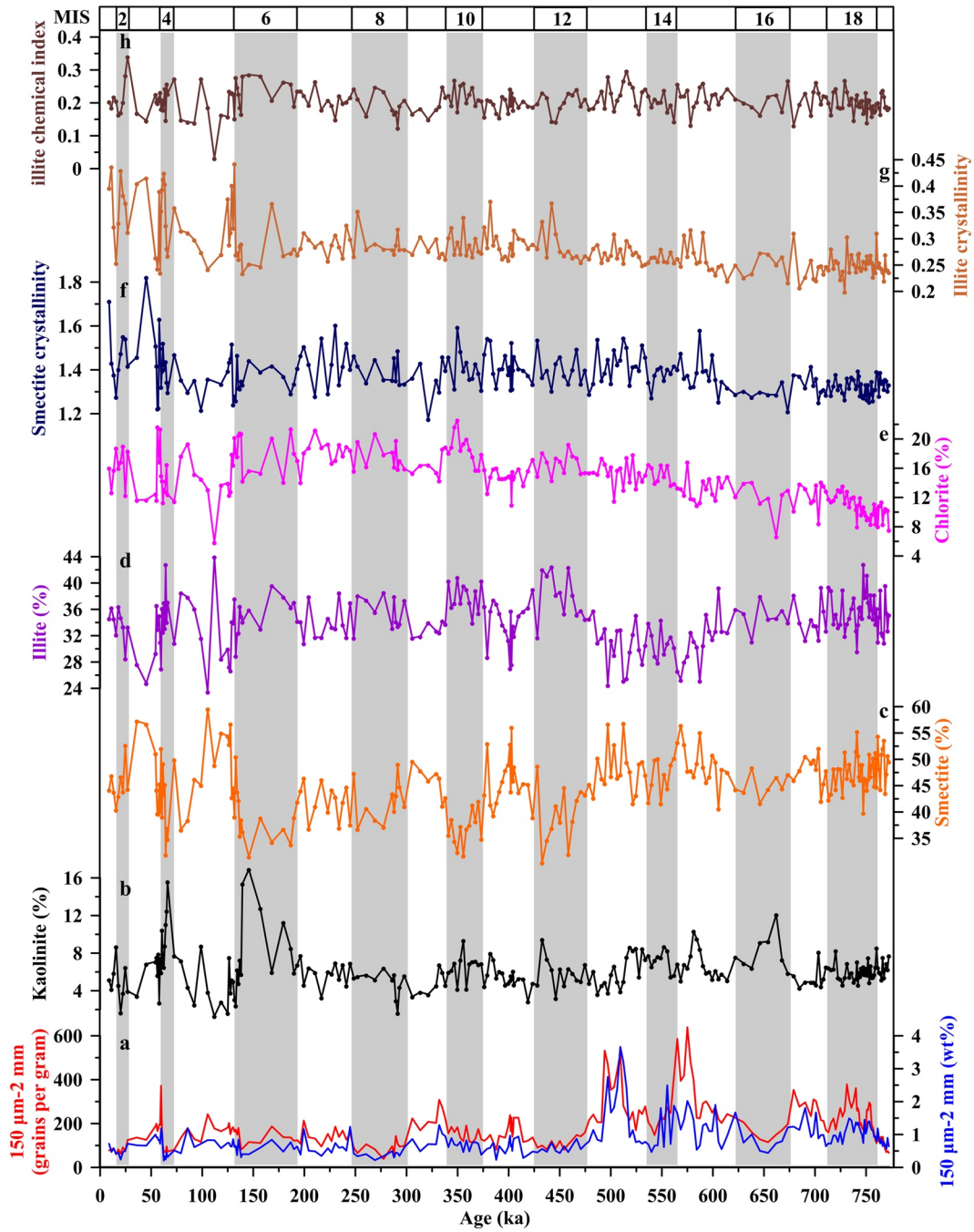


**Figure 3.** Records of (a) iceberg-rafted debris content (grains/g and wt%) and (b–h) clay mineralogy and clay chemistry in core ANT34/A2-10. The gray bars indicate glacial periods, which are numbered with Marine Isotope Stage numbers along the top.

### 4.2. Variability in Clay Mineralogy and Clay Chemistry

The clay-sized fraction of core ANT34/A2-10 consists mostly of smectite (30%–59%) and illite (23%–44%), whereas chlorite (5%–22%) and kaolinite (1%–16%) are less abundant (Figures 3b–3e). In general, the range of variability in chlorite and kaolinite contents is relatively small (~15%) compared to the variability in smectite (~30%) and illite (~20%), but it is nevertheless beyond the analytical limits (±5%) of the method (S. Wan et al., 2017). The kaolinite content shows peaks during certain glacial periods (MIS 4, 6, and 16), but there are otherwise no clear glacial/interglacial trends for kaolinite (Figure 3b). Similarly, there are no clear

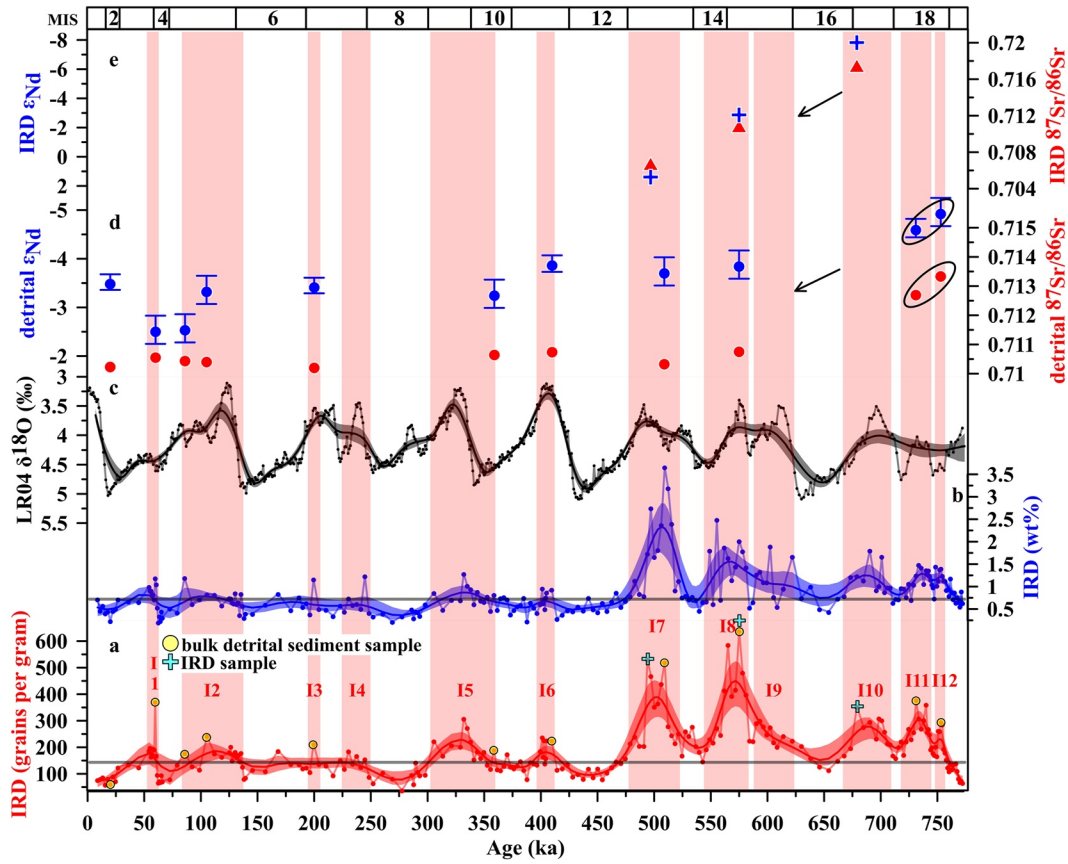


**Figure 4.** Records of iceberg-rafted debris (IRD) content and Sr-Nd isotopic data from selected IRD peak intervals in core ANT34/A2-10. Records of (a) IRD abundance (grains/g), (b) IRD abundance (wt%), and (c) LR04 benthic $\delta^{18}O$ stack are shown with 95% bootstrap confidence intervals, calculated using a "loess" smoothing method and 1,000 bootstrap simulations in Acycle (M. S. Li et al., 2019). The IRD peaks are shaded red and labeled I1-I12, where "I" represents IRD peak. The gray lines in panels (a and b) indicate the average IRD content in the glacial intervals of the record (i.e., 146 grains/g in panel (a) and 0.74 wt% in panel (b)). The yellow circles and green crosses in panel (a) indicate the samples analyzed for Sr-Nd isotopes in bulk detrital sediments (plotted in panel (d)) and IRD grains (plotted in panel (e)). For Nd isotopes, uncertainties (2 SD) are plotted as error bars or are smaller than the symbol size where not shown. For Sr isotopes, uncertainties are smaller than the symbol size for all samples. Glacial periods are numbered with Marine Isotope Stage numbers along the top.

glacial/interglacial trends for chlorite content (Figure 3e). In contrast, smectite and illite content show consistent high-amplitude fluctuations throughout the core, extending back to ~770 ka, with elevated smectite contents during interglacials and elevated illite contents during glacials (Figures 3c and 3d).

Smectite and illite crystallinity values show only minor fluctuations before MIS 6, but exhibit higher frequency and higher amplitude fluctuations since MIS 6 (Figures 3f and 3g). The smectite and illite crystallinity values range from 1.17 to 1.82 $\Delta°2\theta$ (average 1.38) and 0.20 to 0.44 $\Delta°2\theta$ (average 0.28), respectively, indicating high to moderate crystallinity for smectite and very high to high crystallinity for illite (Figures 3f and 3g; Ehrmann et al., 2005). The illite chemical index is consistently less than 0.3, with an average of 0.21, indicating strong physical rock weathering in the source area (Figure 3h; Ehrmann, 1998; Gingele et al., 1998; S. Wan et al., 2006). Furthermore, glacial/interglacial trends in clay mineralogy and chemical parameters (Figures 3b–3h) show systematic variations that coincide with the IRD peak intervals (Figure 3a), with high IRD content generally coinciding with high smectite and low illite content.

### 4.3. Detrital Strontium and Neodymium Isotopes

The Sr and Nd isotopic compositions of bulk detrital samples and the IRD samples (>250 μm) from the IRD peak intervals (sampling shown on Figure 4a) are reported in Table 1. The bulk detrital Sr-Nd isotopic compositions

range from $^{87}Sr/^{86}Sr = 0.710267–0.713400$ and $\varepsilon_{Nd} = -2.5$ to $-5.0$. The IRD sample compositions range from $^{87}Sr/^{86}Sr = 0.707030–0.717786$ and $\varepsilon_{Nd} = +1.2$ to $-8.0$. As such, the IRD samples show a greater range of isotopic variability between samples, and typically differ from the contemporaneous bulk detrital sediment, but both records indicate similar trends through time (Figures 4d and 4e). Before MIS 16, $^{87}Sr/^{86}Sr$ values were higher (more radiogenic), and $\varepsilon_{Nd}$ values were lower (less radiogenic) in both fractions compared to the interval since MIS 16 (Figures 4d and 4e). We also note that the bulk detrital Sr-Nd isotope signature of the glacial MIS 2 sample ($^{87}Sr/^{86}Sr = 0.710295$, $\varepsilon_{Nd} = -3.5$) is within the range of bulk detrital samples from the interglacial IRD peak intervals after MIS 16 ($^{87}Sr/^{86}Sr = 0.710267–0.710815$, mean of 0.710571; $\varepsilon_{Nd} = -2.5$ to $-3.9$, mean of $-3.3$).

## 5. Discussion

### 5.1. Interpretation of the IRD Record

The abundance of IRD in Southern Ocean sediment cores is usually considered to reflect Antarctic Ice Sheet dynamics (Kanfoush et al., 2000; Nielsen et al., 2007; L. Wu, Wilson, et al., 2021; Wilson et al., 2018). However, the IRD content is a mixed signal that is ultimately determined by the flow of icebergs containing debris but that gets further modulated by transport processes and climate; as such, it is not a direct record of ice margin instability. Close to Antarctica, and depending on the local setting, IRD deposition is generally highest during deglacial and interglacial ice-sheet retreat (Hillenbrand et al., 2021; Weber et al., 2014; Wilson et al., 2018) or during glacial ice-sheet advance and collapse (Hillenbrand et al., 2002, 2009; L. Wu, Wilson, et al., 2021). Nevertheless, apart from iceberg calving rates, IRD records can also be influenced by other factors, such as iceberg trajectories, iceberg drift distance, sea surface temperatures, and variable debris content linked to different iceberg source areas (e.g., L. Wu, Wilson, et al., 2021 and references therein), which need to be considered on a site-by-site basis.

Modern icebergs travel anti-clockwise around Antarctica within the Antarctic Coastal Current (Gladstone et al., 2001). The Coriolis force helps to keep them entrained in that current close to the edge of the Antarctic continent (K. L. Smith, 2011), although topographically steered ocean currents allow some of them to stray north (Weber et al., 2021). A similar trajectory probably existed during previous interglacial periods because the Antarctic continental margin geographically constrains the SBACC in the Amundsen Sea sector (Yamazaki et al., 2021; Figure 1b), while the easterly winds driving the Antarctic Coastal Current are largely insensitive to climate (Weber et al., 2021).

Ocean thermal forcing could have induced enhanced ice melting at the grounding line at times of warm CDW or MCDW incursion, but this process would not have significantly influenced the mass loss of drifting icebergs. Icebergs may lose some mass during long-distance drifting (e.g., through wave erosion, friction, or sea-ice collisions), but the mass-loss rates remain low until they reach the warmer waters of the ACC (Weber et al., 2021). Site ANT34/A2-10 is located close to the SBACC, so debris-laden icebergs from the Ross and Amundsen Seas (Hillenbrand et al., 2002) could readily survive to reach site ANT34/A2-10, even under slightly warmer global climate states than modern, before their melting rate increases and they release most of their debris in response to the warmer sea surface temperatures of the ACC.

Whereas elevated IRD contents during the past interglacials probably reflect enhanced calving, the lower IRD content of glacial intervals could be explained by a combination of both restricted iceberg calving under colder Antarctic temperatures and reduced iceberg melt rates during transport in colder waters. At such times, icebergs may have survived transport to more distal locations at lower latitudes (Bigg, 2020). In addition to regional cooling, an equatorward shift of the SWW during colder intervals could have led to the northward migration of the SBACC and SACCF (Civel-Mazens et al., 2021). This scenario could cause local sea surface temperatures at site ANT34/A2-10 to be as cold as those in the Antarctic Coastal Current, thereby increasing the iceberg survivability and decreasing the amount of debris released as they pass site ANT34/A2-10.

It is also important to consider that icebergs derived from different settings (e.g., Alpine-style glaciers vs. large ice shelves) may contain very different IRD contents (J. A. Smith et al., 2019; J. B. Anderson, 1999). Of relevance to the present study is that Alpine-style glaciers from the hinterlands along Dry Valleys/North Victoria Land, Ruppert and Hobbs Coasts, Marie Byrd Land, and the Antarctic Peninsula (Figure 1) contain significant supraglacial/englacial debris, so past retreat of the marine-based WAIS would be expected to lead to a major discharge of debris-laden icebergs. As such, we consider that the IRD content should be a useful marker for large-scale

instabilities, while being relatively insensitive to changes in the ice shelves, since these tend to release relatively debris-free icebergs. Isotopic provenance analysis can also be used to place constraints on how changes in iceberg sourcing could have affected the IRD records.

Although intense ACC flow speeds, particularly during past interglacials (Toyos et al., 2020; Figure 5c), could potentially remove silt and clay particles and thus concentrate particles in the >150 μm size fraction, site ANT34/A2-10 is bathed by AABW and hence should be insensitive to such a direct influence from the ACC (Figure 1b). Furthermore, there is also no evidence for a strong winnowing influence on the record, because sedimentation rates during interglacial IRD peak intervals do not appear unusually low (Figure 2). Therefore, although we have not calculated IRD mass accumulation rates, we consider the abundance of 150 μm-2 mm particles (counts/g or wt%) to be a robust proxy indicator of IRD inputs to this core. In addition, this site is sufficiently far from the Antarctic continental margin (Figure 1) to prevent a single outlet glacier or a single iceberg dumping event from exerting a major control on the IRD records, while a minimal influence from turbidity currents is also envisaged based on its relatively distal setting and the regional seafloor bathymetry (Figure 1b). Previous studies from the adjacent site PS58/254 indicate that its IRD record contains significant orbital variations, thereby confirming that iceberg calving in the study area is not simply a stochastic process (Hillenbrand et al., 2009). Therefore, we suggest that the IRD abundance peaks in core ANT34/A2-10, which occurred predominantly during interglacials (Figure 5a), were driven by increased iceberg fluxes related to the past instability of the WAIS.

### 5.2. Clay Mineral Provenance Changes Driven by Ocean Current Strength

Two important assumptions in interpreting past clay mineral variations in the study area are that the clays are overwhelmingly sourced from the Antarctic region (Hillenbrand & Ehrmann, 2005; Perez et al., 2021) and that modern potential source areas (PSAs) are a good indication of past sources. Stability of source areas is a reasonable approximation for the period of interest (i.e., since ~770 ka) given a lack of notable tectonic activity in Antarctica since the early Pleistocene (Hillenbrand & Ehrmann, 2005; Perez et al., 2021). Our interpretation of a dominant Antarctic source of clay minerals is also supported by the narrow range of smectite crystallinity (1.17–1.82 $\Delta°2\theta$), illite crystallinity (0.20–0.44 $\Delta°2\theta$), and illite chemical index (0.12–0.34) in core ANT34/A2-10 (Figures 3f–3h), which are consistent with derivation from a cold and arid environment. Notably, these values are comparable to the smectite and illite crystallinity and illite chemical index in clays from the Transantarctic Mountains, which range from 0.68–2.87 $\Delta°2\theta$, 0.20–0.94 $\Delta°2\theta$, and 0.05–1.75, respectively (Ehrmann et al., 2005). They are also comparable to the illite crystallinity and chemical index in coretop samples of West Antarctic continental margin clays, which range from ~0.3–0.6 $\Delta°2\theta$ and ~0.1–0.55, respectively (Ehrmann et al., 2011; S. Wu et al., 2019).

In the study area, clay minerals are transported into the marine environment both by entrainment in ocean currents and by drifting sediment-laden icebergs (Hillenbrand et al., 2002), with little dust input from the West Antarctic (Petschick et al., 1996). Site ANT34/A2-10 is sufficiently far from the hinterland of the Bellingshausen, Amundsen, and Ross Seas (Figure 1a) that clay minerals are not supplied directly by glaciers, but via transport in the vigorous ACC and in sediment-laden icebergs. Therefore, past changes in the ACC, or in iceberg provenance and trajectories, could influence the clay mineral assemblages in the core.

We use a ternary diagram with endmembers of (smectite + kaolinite)-illite-chlorite to identify the provenance of clay minerals at site ANT34/A2-10 by comparison to PSAs from the Pacific sector of Antarctica, including the relatively proximal Amundsen and Bellingshausen Seas, the West Antarctic Peninsula to the east, and the Ross Sea and East Antarctica to the west (Figure 6a). The clay mineral assemblages in core ANT34/A2-10 lie close to the clay endmembers from the Amundsen, Bellingshausen, and Ross Seas, suggesting their derivation from a mixture of these sources, while the chlorite content is too low to accommodate a significant West Antarctic Peninsula source (Figure 6a). During glacial intervals with low IRD content, the clay mineralogy is well-explained by mostly local sources from the Amundsen and Bellingshausen Seas (probably dominated by the Amundsen Sea). In contrast, the interglacial IRD peak intervals were accompanied by a clear trend toward higher smectite + kaolinite content, consistent with clays supplied from a region to the west of site ANT34/A2-10, such as the WRS (e.g., CRP-1; Ehrmann et al., 2005) and/or offshore Adelie Land in East Antarctica (e.g., Site U1359; Pant et al., 2013; Figure 6a), which are located upstream in the pathway of the ACC relative to site ANT34/A2-10. The clays in the WRS Embayment initially originated from the Transantarctic Mountains and are enriched in smectite with very low kaolinite contents (Ehrmann et al., 2005), while the Amundsen Sea and

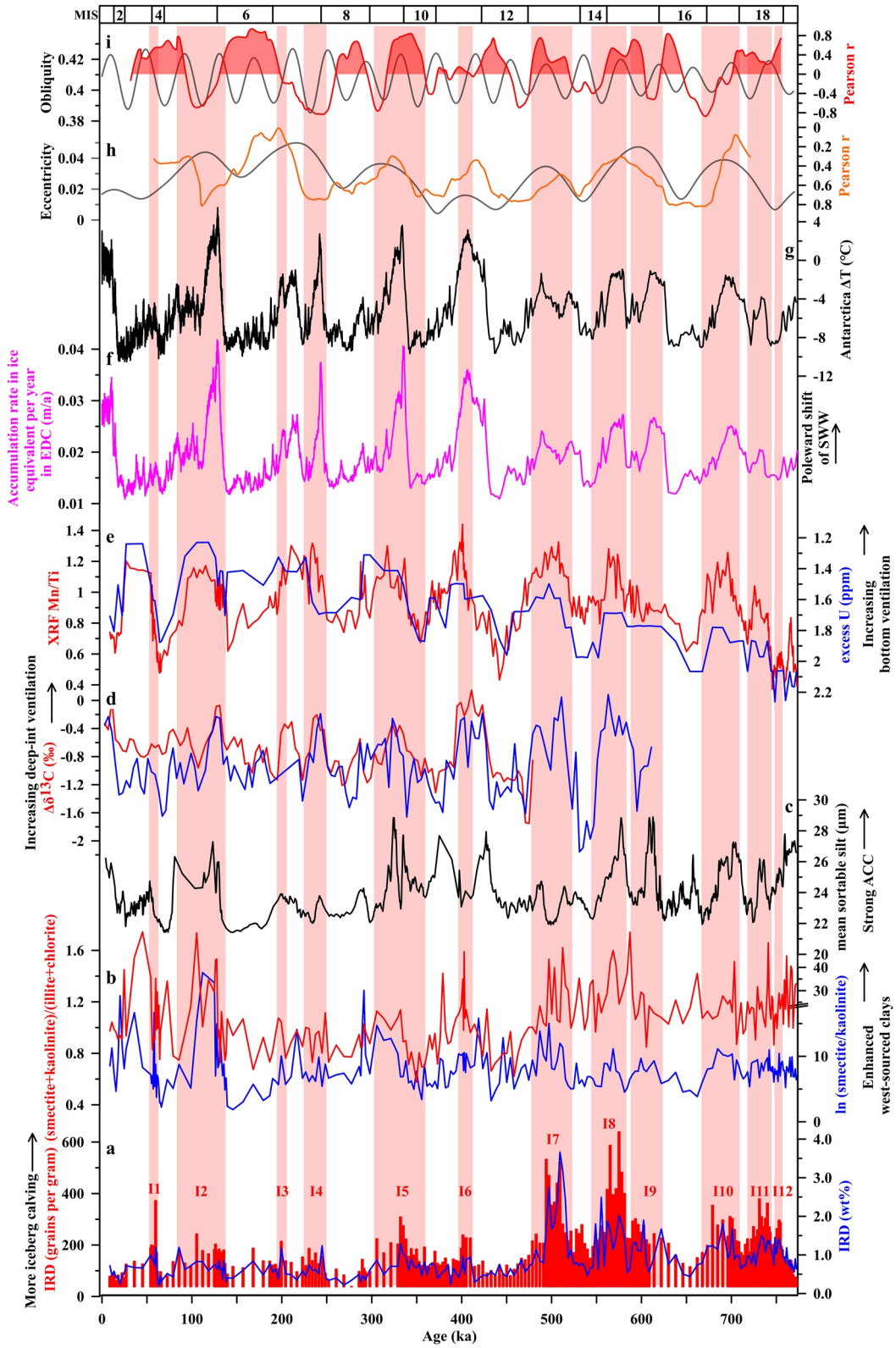
MIS
2
4
6
8
10
12
14
16
18
i
Obliquity
Pearson r
h
Eccentricity
Pearson r
g
Antarctica ΔT (°C)
f
Accumulation rate in ice equivalent per year in EDC (m/a)
Poleward shift of SWW
e
XRF Mn/Ti
excess U (ppm)
Increasing bottom ventilation
d
Increasing deep-int ventilation
Δδ13C (‰)
c
mean sortable silt (μm)
Strong ACC
b
(smectite+kaolinite)/(illite+chlorite)
ln (smectite/kaolinite)
Enhanced west-sourced clays
a
More iceberg calving
IRD (grains per gram)
IRD (wt%)
I1
I2
I3
I4
I5
I6
I7
I8
I9
I10
I11
I12
Age (ka)

**Figure 5.**

Bellingshausen Sea sources have lower smectite content and more kaolinite, as well as a higher illite content (Ehrmann et al., 2011; Hillenbrand et al., 2003). Although the clay mineral assemblages in Pleistocene sediment from Site U1359 (Pant et al., 2013) show higher smectite + kaolinite values than sediments from the Amundsen and Bellingshausen Seas, they are not sufficiently high on their own to explain the values recorded in core ANT34/A2-10 (Figure 6a), while their smectite/kaolinite ratios are too low for them to be a major contributor to ANT34/A2-10. Overall, we consider that both smectite/kaolinite and (smectite + kaolinite)/(illite + chlorite) ratios could provide a tracer for west-sourced clays relative to local clay inputs, and suggest that the former could reflect a mixture of predominantly Ross Sea with potentially some East Antarctic sources.

A recent study indicates a high smectite and illite content in surface sediments from Terra Nova Bay, adjacent to Victoria Land in the WRS (Figure 1a), which were linked to sources from its surrounding volcanic rocks and glacial meltwater, respectively (Figure 6a; Jung et al., 2021). However, the clay mineral compositions recorded during both glacial and interglacial intervals in core ANT34/A2-10 are quite different from the clay mineral endmember in Terra Nova Bay (Figure 6a). A lack of sediment input to ANT34/A2-10 from this source is probably due to the deep channel in Terra Nova Bay (Jung et al., 2021), which may trap fine-grained detritus and minimize its transport out of the Ross Sea. Moreover, the outlet glaciers draining into McMurdo Sound and the Dry Valleys (adjacent to the CRP-1 core) could provide a greater input to the Ross Sea than the more localized outlet glaciers supplying Terra Nova Bay, so that it may be variability in those inputs that drives the variability in our clay mineral record at times when the Ross Ice Shelf has significantly retreated.

In another recent study, Andrews and LeMasurier (2021) presented data indicating average smectite/kaolinite and (smectite + kaolinite)/(illite + chlorite) ratios of ~4.6 and ~0.6, respectively, for surface sediments from the overall Ross Sea, while Marschalek et al. (2021) revealed average smectite/kaolinite and (smectite + kaolinite)/(illite + chlorite) ratios of ~6 and ~0.7, respectively, for Pleistocene sediments from Core U1521 in the central Ross Sea. These results are distinguishable from the average clay mineral composition of surface sediments in the Amundsen Sea (smectite/kaolinite ratio of ~1.1 and (smectite + kaolinite)/(illite + chlorite) ratio of ~0.6) and Bellingshausen Sea (smectite/kaolinite ratio of ~1.9 and (smectite + kaolinite)/(illite + chlorite) ratio of ~0.5). Therefore, these studies appear to further support our interpretation of these clay mineral ratios in terms of clay mineral provenance changes between the more proximal sources in the Amundsen and Bellingshausen Seas and the more distal sources to the west.

We compare the temporal changes in the smectite/kaolinite and (smectite + kaolinite)/(illite + chlorite) ratios at site ANT34/A2-10 (Figure 5b) with the sortable silt record from core PS97/93-2 (Figure 5c), which is located in the pathway of the ACC in the Pacific sector of the Southern Ocean but further downstream (Figure 1a; Toyos et al., 2020). This comparison reveals a clear correlation between the sortable silt and clay mineralogy records, indicating that stronger eastward ACC transport during interglacials was associated with increased inputs from westerly sources such as the Ross Sea, that is, higher smectite/kaolinite and (smectite + kaolinite)/(illite + chlorite) ratios (Figures 5b and 5c). As a corollary, weaker ACC flow during glacial periods would have supplied less west-sourced clay to our site, leading to a greater dominance of more local terrigenous inputs with higher kaolinite content derived from the Amundsen Sea shelf. The supply of such material to the Amundsen Sea continental slope during Late Pleistocene glacial periods when terrigenous ice crossed the Amundsen Sea shelf has previously been proposed, based on the observation of low smectite/kaolinite ratios in fine-grained (<2 μm) detrital sediment records from that region (Hillenbrand et al., 2002, 2003). In addition, contour currents of the glacial Ross Sea Bottom Water may have provided a mechanism to help deliver this low smectite/kaolinite signal from the continental margin of the Amundsen Sea to site ANT34/A2-10.

**Figure 5.** Comparison of iceberg-rafted debris (IRD) and clay mineral proxies in core ANT34/A2-10 to regional paleoceanographic and paleoclimatic records and orbital forcing. (a) IRD proxies in core ANT34/A2-10. The red bars indicate IRD peak intervals, labeled I1 to I12. (b) Clay mineral ratios of smectite/kaolinite (blue line; logarithmic scale) and (smectite + kaolinite)/(illite + chlorite) (red line) in core ANT34/A2-10. (c) Mean sortable silt in core PS97/93-2, based on XRF 5-point smoothed Zr/Rb transformation (Toyos et al., 2020). (d) Benthic $\delta^{13}C$ gradient between the Southeast Pacific Rise—intermediate South Atlantic ($\Delta\delta^{13}C_{(PS75/059\text{-}2\text{-}ODP1088)}$; red line), and deep South Atlantic—intermediate South Atlantic ($\Delta\delta^{13}C_{(ODP1089\text{-}ODP1088)}$; blue line), based on data from (Hodell et al., 2003; Ullermann et al., 2016). The original time series were resampled at a 4 kyr spacing with linear interpolation between data points before calculating the gradients. (e) XRF Mn/Ti (red line) and excess U (blue line, reversed axis) in core ANT34/A2-10 (Tang et al., 2022). (f) Accumulation rate in ice equivalent per year in the EPICA Dome C (EDC) ice core (Wolff et al., 2010). (g) Temperature anomaly in the EDC ice core (Jouzel et al., 2007). (h) Eccentricity (gray line) and correlation coefficient (Pearson *r*) between eccentricity and IRD abundance over a 100 kyr sliding window (orange line). (i) Obliquity (gray line) and correlation coefficient between obliquity and IRD abundance over a 40 kyr sliding window (red line, shaded when Pearson $r > 0$). The program "Past V3.5" (Hammer & Harper, 2008) was used to resample these data. The orbital parameters are from Laskar et al. (2004). Glacial periods are numbered with Marine Isotope Stage numbers along the top.

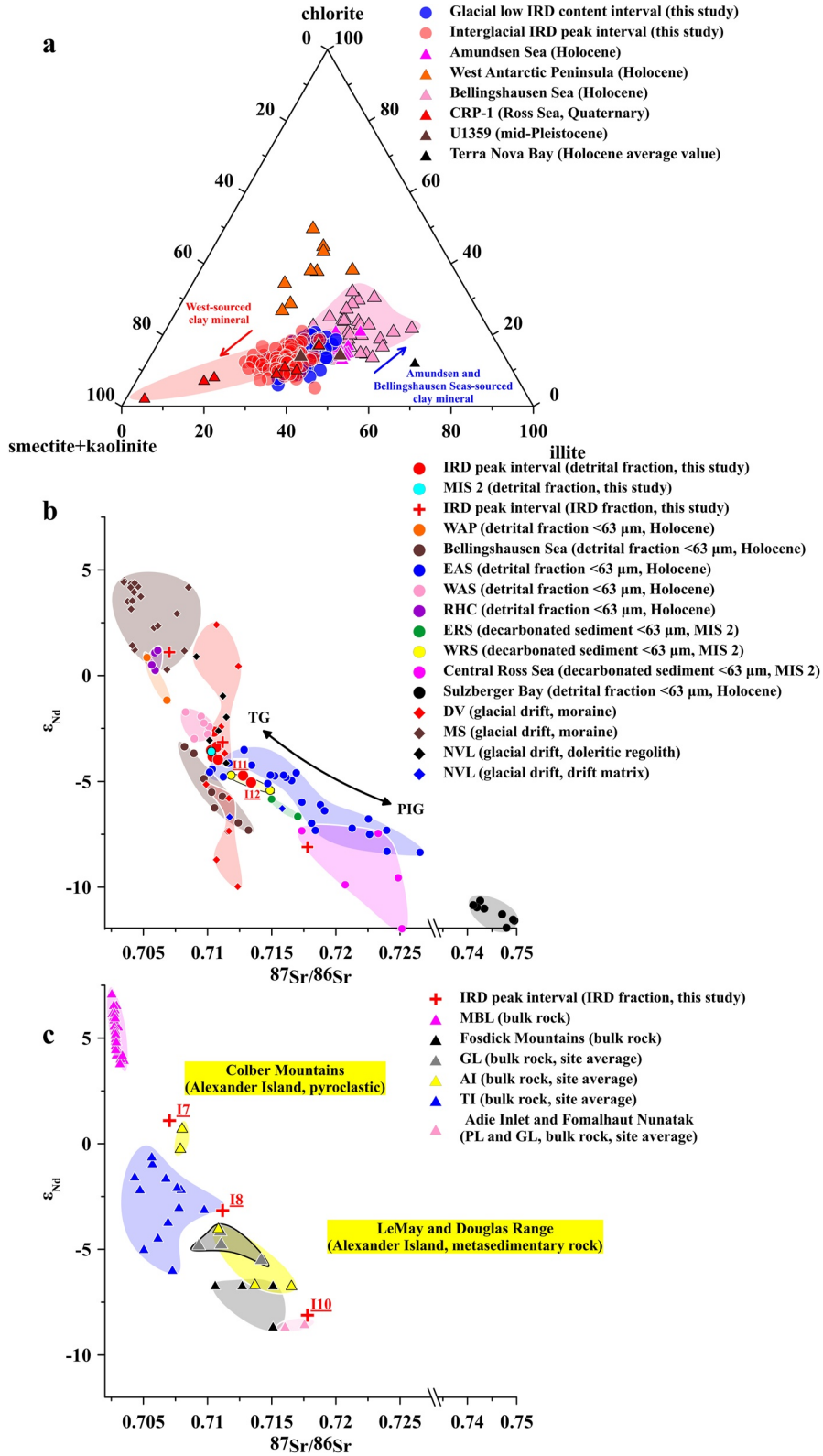
a
chlorite
smectite+kaolinite
illite
West-sourced clay mineral
Amundsen and Bellingshausen Seas-sourced clay mineral
Glacial low IRD content interval (this study)
Interglacial IRD peak interval (this study)
Amundsen Sea (Holocene)
West Antarctic Peninsula (Holocene)
Bellingshausen Sea (Holocene)
CRP-1 (Ross Sea, Quaternary)
U1359 (mid-Pleistocene)
Terra Nova Bay (Holocene average value)
b
TG
PIG
I11
I12
87Sr/86Sr
IRD peak interval (detrital fraction, this study)
MIS 2 (detrital fraction, this study)
IRD peak interval (IRD fraction, this study)
WAP (detrital fraction <63 μm, Holocene)
Bellingshausen Sea (detrital fraction <63 μm, Holocene)
EAS (detrital fraction <63 μm, Holocene)
WAS (detrital fraction <63 μm, Holocene)
RHC (detrital fraction <63 μm, Holocene)
ERS (decarbonated sediment <63 μm, MIS 2)
WRS (decarbonated sediment <63 μm, MIS 2)
Central Ross Sea (decarbonated sediment <63 μm, MIS 2)
Sulzberger Bay (detrital fraction <63 μm, Holocene)
DV (glacial drift, moraine)
MS (glacial drift, moraine)
NVL (glacial drift, doleritic regolith)
NVL (glacial drift, drift matrix)
c
Colber Mountains (Alexander Island, pyroclastic)
LeMay and Douglas Range (Alexander Island, metasedimentary rock)
I7
I8
I10
IRD peak interval (IRD fraction, this study)
MBL (bulk rock)
Fosdick Mountains (bulk rock)
GL (bulk rock, site average)
AI (bulk rock, site average)
TI (bulk rock, site average)
Adie Inlet and Fomalhaut Nunatak (PL and GL, bulk rock, site average)

**Figure 6.**

### 5.3. Provenance Changes of Detrital Sr-Nd Isotopes Related to High-Latitude Ocean-Atmosphere-Ice Sheet Processes

#### 5.3.1. Detrital Sr-Nd Isotopic Signature Since MIS 16

The Sr-Nd isotopic composition of bulk detrital sediments and IRD samples in ANT34/A2-10 are compared to data from regolith, glacial drift, sediment detrital fractions (<63 μm), and bulk rocks representing PSAs from the Antarctic margin in the South Pacific sector in Figures 6b and 6c. This comparison allows us to determine the possible terrigenous sources to this site, and ultimately their relation through time to oceanic and atmospheric circulation patterns.

Overall, the detrital continental margin sediments reflecting the PSAs of West Antarctica (circles in Figure 6b) have $\varepsilon_{Nd}$ values ranging from −11.9 to +1.3 and $^{87}Sr/^{86}Sr$ ratios ranging from 0.705 to 0.750 (Simões Pereira et al., 2018, 2020). Note that there is also heterogeneity between samples collected from different locations within a given coastal region. For example, detrital sediments in the Eastern Amundsen Sea (EAS) have a range of $^{87}Sr/^{86}Sr$ ratios from 0.710 to 0.727, with $\varepsilon_{Nd}$ values between −8.3 and −3.4, while detrital sediments in the Western Amundsen Sea (WAS) have a narrower range of $^{87}Sr/^{86}Sr$ ratios from 0.708 to 0.710, with $\varepsilon_{Nd}$ values between −2.9 and −1.7 (Figure 6b). These differences reflect the different sediment sources to the WAS and EAS, with detritus in the WAS sourced from Mesozoic coastal granites, while bedrock or sediment-fill beneath the Pine Island Glacier and Thwaites Glacier are the main sources of sediment to the EAS (Simões Pereira et al., 2018, 2020). The Sr-Nd isotope signatures in the EAS (Figure 6b) are also sensitive to contributions from Pine Island Glacier (low $\varepsilon_{Nd}$ values, high $^{87}Sr/^{86}Sr$ ratios) versus Thwaites Glacier (higher $\varepsilon_{Nd}$ values, lower $^{87}Sr/^{86}Sr$ ratios; Simões Pereira et al., 2018, 2020). For the Ross Sea, decarbonated sediment in the Eastern Ross Sea (ERS) yields $^{87}Sr/^{86}Sr$ ratios of 0.715–0.717, with $\varepsilon_{Nd}$ values between −6.6 and −5.8, while the WRS and the central Ross Sea are characterized by $^{87}Sr/^{86}Sr$ ratios of 0.712–0.715 and 0.717 to 0.725, with $\varepsilon_{Nd}$ values ranging from −5.4 to −4.6 and −11.9 to −7.3, respectively (Figure 6b; Farmer et al., 2006). Sediments in the ERS are influenced by proximal sources in West Antarctica and the southern Transantarctic Mountains, while the Late Cenozoic McMurdo Volcanics provide a sediment source to McMurdo Sound and the WRS (Farmer et al., 2006; Figure 6b). A wide range of isotopic compositions is also observed in the detrital fraction of the marginal seas further to the east (the Bellingshausen Sea and West Antarctic Peninsula), with $^{87}Sr/^{86}Sr$ ratios ranging from 0.705 to 0.713, and $\varepsilon_{Nd}$ between −7.2 and +0.9 (Figure 6b; Simões Pereira et al., 2018). In contrast, the detrital fraction from offshore of the Ruppert and Hobbs Coasts shows a narrow compositional range, with low $^{87}Sr/^{86}Sr$ ratios from 0.7056 to 0.7061 and high $\varepsilon_{Nd}$ values between +0.3 and +1.3 (Simões Pereira et al., 2018; Figure 6b), reflecting detrital inputs from the coastal Late Cenozoic alkali basalts and Cretaceous calc-alkaline granites (Simões Pereira et al., 2018).

The bulk detrital Sr-Nd isotopic compositions analyzed from IRD peak intervals since ~620 ka (I1, I2, I3, I5, I6, I7, and I8) and from MIS 2 (~20 ka) in core ANT34/A2-10 (Table 1) lie close to the signatures of the EAS (Thwaites Glacier), WAS, WRS, and Bellingshausen Sea (Figure 6b). Hence, these data appear to implicate a mixture of sediments from some combination of those marginal seas. In principle, transport could occur by grounded ice flow and turbidity currents from those shelf regions to the continental rise (J. B. Anderson et al., 1984; Lowe & Anderson, 2002), followed by bottom current reworking and redeposition on the deep continental rise. Since the bottom contour current and the ACC experienced significant variations during glacial/interglacial cycles, these mechanisms might be expected to have generated differences in the proportions of sediment derived from different PSAs through time. For example, the clay mineralogy results suggest that a weak ACC and vigorous AABW

**Figure 6.** Sediment provenance analysis of clay minerals and Sr-Nd isotopes in core ANT34/A2-10. (a) Ternary diagram of (smectite + kaolinite)-illite-chlorite, showing clay mineral compositions in core ANT34/A2-10 during glacial intervals with low iceberg-rafted debris (IRD) content and during IRD peaks within interglacial periods, and a comparison to published clay data. (b) Sr-Nd isotopic compositions of bulk detrital sediment and IRD samples (>250 μm) in core ANT34/A2-10 from IRD peak intervals and one bulk detrital sediment sample from Marine Isotope Stage 2, compared to published detrital Sr-Nd data. (c) Sr-Nd isotopic compositions of IRD samples in core ANT34/A2-10 during IRD peak intervals compared to published bulk rock Sr-Nd isotopic data from selected West Antarctic sources. Note the break of scale on the *x* axis for panels (b and c). Endmember data for clay minerals are from previous studies (Diekmann et al., 2004; Ehrmann et al., 2005, 2011; Hillenbrand, 2000, 2001; Hillenbrand et al., 2003; Jung et al., 2021; Pant et al., 2013; Setti et al., 2004). Sr-Nd isotope data are from previous studies (Adams et al., 2005; Blakowski et al., 2016; Farmer et al., 2006; Futa & Le Masurier, 1983; Hart et al., 1997; Korhonen et al., 2010; McCarron & Smellie, 1998; Pankhurst et al., 1993; Riley et al., 2001; Ryan, 2007; Simões Pereira et al., 2018, 2020). Abbreviations: AI, Alexander Island; CRP-1, Cape Roberts Project-1; DV, Dry Valleys; EAS, Eastern Amundsen Sea; ERS, Eastern Ross Sea; GL, Graham Land; MBL, Marie Byrd Land; MS, McMurdo Sound; NVL, North Victoria Land; PIG, Pine Island Glacier; PL, Palmer Land; RHC, Ruppert and Hobbs Coasts; TG, Thwaites Glacier; TI, Thurston Island; WAP, West Antarctic Peninsula; WAS, Western Amundsen Sea; WRS, Western Ross Sea.

flow during the last glacial period at ~20 ka (Basak et al., 2018; S. Wu, Lembke-Jene, et al., 2021) could have led to less Ross Sea-sourced and more Amundsen and Bellingshausen Seas-sourced fine-grained detritus reaching this site compared to during the interglacial IRD peak intervals (Figures 5b and 5c). However, such a difference is not observed in Sr-Nd isotopes, which are similar between these periods (Figures 4d and 6b), which may suggest that deep-ocean current transport had a minor influence on the bulk detrital Sr-Nd isotopic compositions. This scenario could simply reflect the shorter sediment transport distance of the bulk detrital sediment compared to the fine-grained clay fraction, but it could also implicate a more significant (and perhaps dominant) role for icebergs in supplying the coarser detritus (>2 μm) to site ANT34/A2-10.

In addition to the above PSAs, the bulk detrital Sr-Nd isotopic compositions during IRD peak intervals and MIS 2 also overlap with the compositions of glacial drift from the Dry Valleys and North Victoria Land, which show similar Sr isotopic compositions of 0.709–0.712 and a wide range of $\varepsilon_{Nd}$ values between −8.6 and +2.5 (Blakowski et al., 2016) (diamonds in Figure 6b). These results could indicate supply to site ANT34/A2-10 from Alpine-type glaciers in the Dry Valleys/North Victoria Land regions, consistent with the WRS source proposed above. However, it is important to note that it is hard to distinguish these WRS sources from the WAS/EAS sources. The glaciers in the Dry Valleys/North Victoria Land regions would have been advanced into the Ross Sea Embayment in the form of outlet glaciers during glacial periods (Heath et al., 2022), while their retreat during warm periods could supply such glacial drift via calving icebergs. Overall, the consistent Sr-Nd isotope signatures since MIS 16 implicate a mixture of terrigenous detritus supplied predominantly by icebergs from the Amundsen and Bellingshausen Seas and from the Dry Valleys/North Victoria Land (WRS) that probably drifted through modern-like iceberg trajectories to our site (Figures 1c and 7a).

This modern-like iceberg trajectory is also supported by comparing the Sr-Nd isotope signature of the IRD in this core (from I7 and I8) to bulk rock PSAs in the South Pacific sector of West Antarctica (Figure 1a). The IRD sample from I8 ($^{87}Sr/^{86}Sr = 0.711$, $\varepsilon_{Nd} = -3.1$) has a similar composition to the contemporaneous bulk detrital sediments, whereas the IRD sample from I7 has considerably lower $^{87}Sr/^{86}Sr$ ratios (0.707) and higher $\varepsilon_{Nd}$ values (+1.2) than the bulk detrital sediment from I7 (but note that these samples were from different core depths; Figure 4a). Overall, these IRD data lie close to the composition of sediments from the West Antarctic margins and the Ross Sea (Figure 6b), as well as specifically matching certain rock endmembers, such as those from Graham Land and Alexander Island (Figure 6c). The more radiogenic Nd and less radiogenic Sr isotope signatures in the I7 sample suggest a dominant volcanic contribution, which could potentially reflect local volcanic sources from Marie Byrd Land (Figure 6c), which influence sediments along the Ruppert and Hobbs Coasts (Figure 6b), or more distal pyroclastic sources from Alexander Island (Figure 6c). Such a mixture of iceberg sources from these PSAs is consistent with modern-like iceberg trajectories after MIS 16 (Figure 7a), with detritus carried northwestward by iceberg rafting from the Amundsen and Bellingshausen Sea Embayments by wind- and tide-driven currents (Hillenbrand et al., 2003; Simões Pereira et al., 2018), with a further potential influence from the westward-flowing Antarctic Coastal Current (Hillenbrand et al., 2003; Simões Pereira et al., 2018; Tournadre et al., 2015).

#### 5.3.2. Detrital Sr-Nd Isotopic Signature Before MIS 16

Rather than a mixed signal from the Ross, Amundsen, and Bellingshausen Sea shelf regions (as seen since MIS 16), the bulk detrital Sr-Nd isotopic compositions from the I11 and I12 peaks (before MIS 16) lie close to the signatures of detrital sediment from the Ross Sea shelf region, specifically overlapping with the WRS sources and trending toward ERS and central Ross Sea sources (Figure 6b). While it is hard to constrain a unique provenance solution given the wide range of variability in the PSAs, the bulk detrital Sr-Nd isotopic compositions from the I11 and I12 peaks may indicate an increased contribution, or possible dominance, of sediment from Ross Sea sources during this time period (Figure 6b). Such a change could reflect the importance of iceberg-delivered detritus, with the shift in provenance arising from differing iceberg trajectories before and after MIS 16. Such changes may relate to a proposed shift in the position of the Amundsen Sea Low (ASL), an important and highly dynamic regional low-pressure system, at ~620 ka (Konfirst et al., 2012; Figure 7).

The ASL is a crucial driver of modern West Antarctic climate variability and controls the meridional winds directed toward West Antarctica (Hosking et al., 2013; Turner et al., 2013; Wang et al., 2020). Furthermore, variability of the ASL may play a role in accelerating glacial ice loss (Hosking et al., 2016), due to its influence on the heat budget (Dotto et al., 2020), the cavity circulation (Hattermann et al., 2021), the upwelling of warm CDW in polynyas (Kim et al., 2021), and the import of CDW beneath the ice shelves (Holland et al., 2019). All those

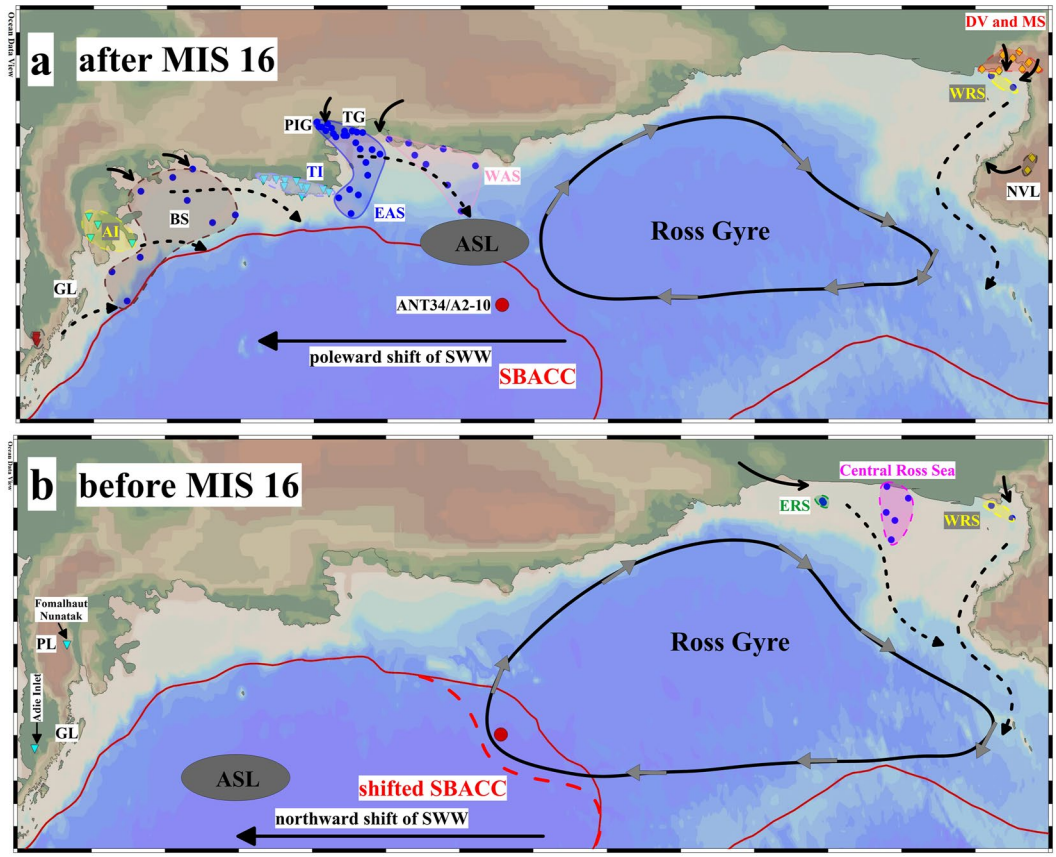


**Figure 7.** Schematic diagram of iceberg trajectories (a) after Marine Isotope Stage (MIS) 16 and (b) before MIS 16. (a) Modern-like iceberg trajectories after MIS 16, shown by black dashed lines, modified from previous studies (England et al., 2020; Gladstone et al., 2001; Simões Pereira et al., 2018; Tournadre et al., 2015). (b) Proposed iceberg trajectories before MIS 16, shown by black dashed lines. We suggest that this interval was characterized by shifts in the Amundsen Sea Low (ASL) and the Southern Boundary of the Antarctic Circumpolar Current (SBACC; red dashed line) and an expansion of the Ross Gyre. The black arrow in panel (a) represents poleward-shifted southern westerly winds (SWW), while the black arrow in panel (b) indicates northward-shifted SWW. For source area abbreviations, see Figure 1 caption.

processes could act to induce ocean-forced ice-sheet instability in this region. Moreover, intensification of the ASL can be linked to a positive Southern Annular Mode (SAM) and poleward migration of the SWW (Hosking et al., 2016; O'Connor et al., 2021; Turner et al., 2013). This situation could generate a negative sea surface height anomaly center in the northeast Ross Sea and be expected to expand and strengthen the Ross Gyre (Dotto et al., 2018), increasing its impact on iceberg trajectories in this region.

Konfirst et al. (2012) suggested that the ASL had a more northeastward and stable annual position before ~620 ka than since that time, which could lead to the negative sea surface height anomaly being centered further northeastward (Figure 7b). We speculate that this condition would have led to a long-term state involving an expanded Ross Gyre, thus favoring transport of coastal icebergs from the Ross Sea Embayment to site ANT34/A2-10 (Figure 7b). Conversely, once a southwestward shift of the ASL established the modern-like southwestward sea surface height anomaly center, a contracted Ross Gyre could explain the mixed pattern of detrital sources from the Ross, Amundsen, and Bellingshausen Seas (Figure 7a). In addition, this latter scenario could lead to enhanced ice-sheet instability in those regions of the WAIS in response to these atmosphere-ocean changes (Steig et al., 2012; Thoma et al., 2008), which could have contributed to the increased supply of IRD from those local WAIS margins since MIS 16.

The Sr-Nd isotope signature of IRD samples was only measured in one sample (I10) from before MIS 16, so any interpretations of that data point should be taken as preliminary. Nevertheless, it shows the same sense of changes as the bulk detrital data from before MIS 16 (i.e., more radiogenic Sr isotopes and less radiogenic

Nd isotopes) (Figures 4d, 4e, and 6c), and overlaps with central Ross Sea sediments (Figure 6b), so could also reflect a dominantly Ross Sea source. In addition, its composition is similar to the signature of Paleozoic/Mesozoic granitoids from Adie Inlet/Fomalhaut Nunatak (Figure 6c), making transport from Palmer Land to site ANT34/A2-10 another possibility. However, it differs from the composition of pyroclastic sources in Alexander Island (Figure 6c), which is the node of iceberg transport from Palmer Land to site ANT34/A2-10, which may argue against this alternative iceberg pathway. More Sr-Nd-Pb isotope data from both detrital and IRD samples from this interval, as well as single-mineral $^{40}Ar/^{39}Ar$ and U/Pb evidence, should be explored to better constrain the changes in iceberg trajectories at this time and test these hypotheses.

### 5.4. Evidence for Ocean-Forced WAIS Instability Since ~770 ka

Today, the incursion of relatively warm CDW and/or MCDW onto the shelf regions in the South Pacific sector of the WAIS (Figure 1b) contributes to the loss of buttressing ice shelves, enhanced drainage of outlet glaciers, and grounding-line retreat, accompanied by iceberg calving (Adusumilli et al., 2020; Das et al., 2020; Hofmann et al., 2012; Lowe & Anderson, 2002; Nakayama et al., 2018; S. S. Jacobs et al., 1996, 2011). These changes in CDW circulation are probably related to latitudinal shifts in the SWW (Hillenbrand et al., 2017; Steig et al., 2012; Thoma et al., 2008), possibly in response to changes in the SAM and teleconnections to the tropical Pacific climate (Steig et al., 2012). This section assesses how past changes in WAIS dynamics evidenced in our IRD and provenance records from core ANT34/A2-10 were related to atmosphere-ocean forcing operating in the Southern Ocean on orbital timescales.

Several proxies have been used to provide evidence of past changes in atmospheric and ocean circulation in the Southern Ocean over orbital timescales. Based on the idea that deepwater stratification in the Southern Ocean would increase the regenerated nutrient content in the deep ocean and reduce the preformed nutrient content in southern-sourced intermediate waters (Toggweiler et al., 2006), benthic foraminiferal $\delta^{13}C$ gradients between the deep and intermediate ocean ($\Delta\delta^{13}C_{deep\text{-}int}$) can be used to reconstruct the vertical chemical stratification (Charles et al., 2010; Hall et al., 2001; Hodell et al., 2003; Ullermann et al., 2016). Meanwhile, reconstructions of sortable silt mean grain size in core PS97/93-2 from the Drake Passage provide a record of ACC strength in the Pacific sector (Toyos et al., 2020), which may be related to changes in the SWW and surface buoyancy forcing (S. Wu, Lembke-Jene, et al., 2021). In addition, the bottom water oxygenation proxies (XRF Mn/Ti and excess uranium) in core ANT34/A2-10 reflect deep Southern Ocean ventilation (Tang et al., 2022), while ice accumulation rates in the EDC ice core provide evidence on SWW-driven upwelling (Fudge et al., 2013).

A comparison of these records reveals a clear correlation in which the IRD peak intervals coincide with reduced benthic $\delta^{13}C$ gradients ($\Delta\delta^{13}C_{deep\text{-}int}$), peaks in EDC ice accumulation rate, elevated mean sortable silt in core PS97/93-2, and shifts in clay mineralogy and bottom water oxygenation proxies in core ANT34/A2-10 (Figures 5a–5f). These results indicate a temporal link between iceberg calving from the WAIS and regional conditions of weak deep stratification, well-ventilated CDW, strengthening ACC, and intense SWW-driven upwelling. Such agreement is consistent with the persistence of an ocean-forced WAIS instability in the South Pacific sector of the Southern Ocean on orbital timescales since at least ~770 ka.

In detail, the co-variation between these proxies supports the hypothesis that during the interglacial periods, a poleward shift in the SWW accompanied by an intensification of the ASL (in accord with positive SAM) (Turner et al., 2013) led to incursions of warm CDW onto the Antarctic shelves, causing grounding line retreat and ice mass loss from the WAIS (Hofmann et al., 2012; Schmidtko et al., 2014; S. S. Jacobs et al., 1996; Thoma et al., 2008; Figure 8a). Furthermore, the influx of meltwater to the surface of the Southern Ocean (England et al., 2020) could have stabilized the upper water column, enabling warming of the stratified subsurface ocean and causing further disintegration of the WAIS (Fogwill et al., 2015; Liu et al., 2015; Menviel et al., 2010; Schmidtko et al., 2014; S. S. Jacobs et al., 2011; Walker et al., 2007; Figure 8a). In addition to local iceberg input from the Amundsen and Bellingshausen Seas, icebergs calved from glaciers in the WRS could have been transported northward by a clockwise Antarctic Coastal Current and then been driven eastward by the SWW to reach site ANT34/A2-10, following modern-like iceberg trajectories (Figure 7a; Baines & Fraedrich, 1988).

The opposite scenario is envisaged during cold glacial periods, when the absence of IRD peaks at site ANT34/A2-10 may have been linked to the deeply stratified Southern Ocean (Wu et al., 2018), weak ACC strength (Toyos et al., 2020; S. Wu, Lembke-Jene, et al., 2021), and northward-shifted SWW that led to reduced

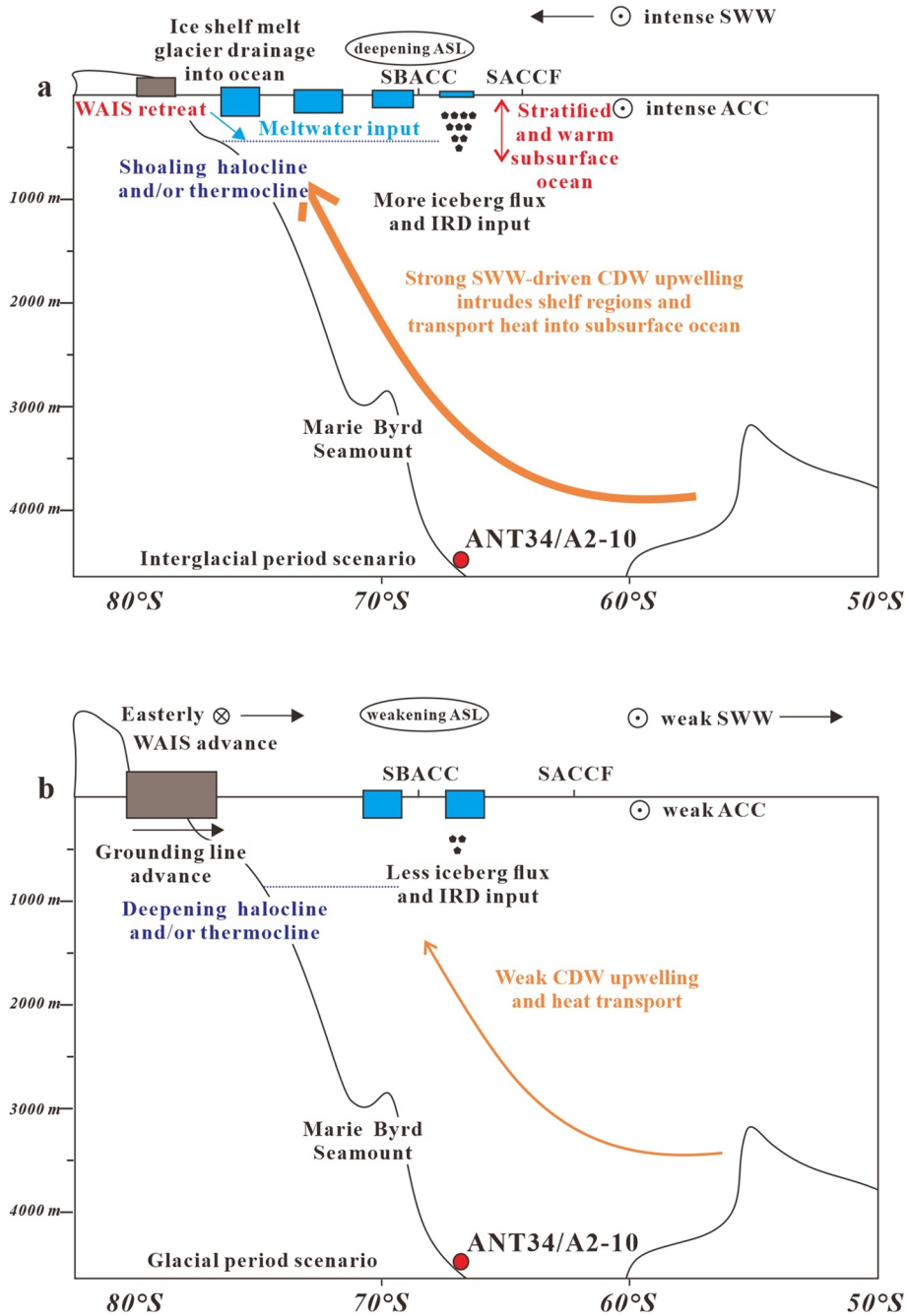


**Figure 8.** Schematic diagram of (a) ocean-forced West Antarctic Ice Sheet instability during iceberg-rafted debris peaks within interglacial periods, compared to (b) more stable glacial conditions. See main text for discussion. The location of the core site is shown with the red dot.

CDW upwelling and weak ocean forcing acting on the WAIS margins, similar to the situation during pre-MIS 16 interglacials (Figure 8b). An additional factor in the weak ocean forcing during glacial periods may have been the suppression of MCDW incursions into the Ross Ice Shelf by the presence of dense shelf waters, related to the strong formation of Ross Sea-sourced AABW (Basak et al., 2018).

### 5.5. Enhanced Instability of the WAIS During MIS 13 and 15

The largest IRD peaks in the record from core ANT34/A2-10 occurred during MIS 13 and MIS 15 (Figure 5a), which may point to a maximum in WAIS instability during this interval. A depositional anomaly during MIS 13–15 was also observed in several sedimentary properties in core PS58/254 from the Amundsen Sea margin (Figures 1a and 1b) and was interpreted in terms of possible retreat or collapse of the WAIS during MIS 13 and MIS 15 (Hillenbrand et al., 2009). In the Antarctic ice core record, those interglacials were cooler than the more recent interglacials since the Mid-Brunhes Event at ~420 ka, and were separated by the unusually short and weak glacial period of MIS 14 (Figure 5g; Hao et al., 2015; Jouzel et al., 2007). Therefore, the relatively warmer conditions during MIS 14 may have contributed to different initial boundary conditions upon the onset of MIS 13 and led to extra ice mass loss during MIS 13. However, it is also possible that the cooler Antarctic temperatures during MIS 13 and MIS 15 than in the more recent interglacial periods could have enhanced iceberg survivability. Whether such an influence could help explain the high IRD peaks (by allowing more icebergs to reach the site), or instead could mean that they represent an under-estimate of iceberg calving changes (by shifting the locus of iceberg melting to lower latitudes) is not known. However, there was no distinct difference in sediment provenance between these interglacials and the more recent interglacials (Figures 4d and 4e), which could point to similar iceberg sourcing and no significant influence of survivability changes, such that the elevated IRD content probably represents greater calving during MIS 13 and MIS 15. The previous glacial history could also matter for sediment supply to icebergs from inland glacial troughs, so the decline in IRD in subsequent interglacial intervals could also partly represent the removal of such debris from glacial troughs during this period of strong instability.

Moreover, the southward movement of the SWW and ASL after ~620 ka (Figure 7a), as previously proposed (Konfirst et al., 2012) and supported by bulk detrital sediment provenance shifts in core ANT34/A2-10 (Figure 4d; Section 5.2.3), may have played a role in the enhanced WAIS instability during MIS 13 and MIS 15, by enabling CDW upwelling near the shelf break (Steig et al., 2012; Thoma et al., 2008). Interestingly, despite the lukewarm nature of MIS 13 and MIS 15 in ice core records (Figure 5g), these intervals were still characterized by small $\Delta\delta^{13}C_{\text{deep-int}}$ gradients in the Southern Ocean (Figure 5d) that were comparable to more recent interglacials, which is consistent with strong deep ocean ventilation and strong ocean forcing during these intervals. Despite cooler interglacial temperatures near the Subantarctic Front during this interval than since the Mid-Brunhes Event (Ho et al., 2012), the surface ocean near Antarctica may have been warmer at this time due to local ocean dynamics (Konfirst et al., 2012). Future work should further investigate ocean temperatures near Antarctica during this interval and their implications for the ice sheet behavior.

Spectral analysis can be used to characterize the pacing of past variability in the IRD inputs from the WAIS and to assess potential links to orbital forcing, as well as whether these aspects changed in relation to the proposed circulation shift at ~620 ka or could explain the enhanced IRD during MIS 13–15. Analysis of the IRD abundance (grains/g) reveals a significant peak in the ~100 kyr eccentricity band, with power also in the ~41 kyr obliquity band (Figure S2a in Supporting Information S1), while the low sedimentation rate and age model uncertainty restrict the potential to resolve power in the precession band. Wavelet analysis of the IRD abundance shows significant power only before ~400 ka in the 41 kyr band, whereas there is significant power in the 100 kyr band throughout the record (Figure S2b in Supporting Information S1).

We also used the "cross wavelet and wavelet coherence toolbox' for MATLAB (Grinsted et al., 2004) to perform cross-wavelet coherence (XWT) analysis between the IRD record and both eccentricity and obliquity (Laskar et al., 2004). For eccentricity, the XWT analysis reveals a significant coherent in-phase relationship with the IRD record in the 100 kyr band (Figure S2d in Supporting Information S1), with no lead or lag resolvable (Figure S2e in Supporting Information S1). Additionally, the correlation coefficient (Pearson *r*) between eccentricity and IRD abundance is above 0 in 100 kyr sliding time windows through the full record (Figure 5h). Except for IRD peaks I2 and I4, the IRD peaks in all other interglacials coincide with a decrease in Pearson *r* and an increase in eccentricity (Figure 5h), which indicates the linkage between warm interglacials and WAIS instability. Variability in the Antarctic Ice Sheet with a period of 100 kyr has previously been inferred for earlier geological intervals (Levy et al., 2019; Patterson et al., 2014) and has typically been linked to a dominance of insolation forcing rather than ocean forcing. However, in the mid to Late Pleistocene, ~100 kyr periodicity could also arise from ocean forcing changes linked to glacial-interglacial cycles. Despite the strong eccentricity during MIS 13 and 15 (Figure 5h), such eccentricity forcing seems unable on its own to explain the anomalously high IRD abundance during these

times, because subsequent intervals with similarly high eccentricity (e.g., MIS 5 and MIS 7; Figure 5h) were not accompanied by such elevated IRD peaks (Figure 5a).

Low obliquity usually relates to cooler surface conditions at high latitudes, enhancing iceberg survivability and leading to contemporaneous IRD peaks in lower latitudes and low IRD signals in high latitudes (Starr et al., 2021). This phenomenon could help explain the linkage between low obliquity, low IRD content, and positive Pearson *r* during glacials in core ANT34/A2-10 (Figure 5i). In contrast, high obliquity is linked to increased annual mean insolation at high latitudes (Loutre et al., 2004), which could drive additional ice mass loss. We observe a positive and significant Pearson *r* between obliquity and IRD abundance during MIS 13 to 15 (Figure 5i), which was accompanied by the most significant coherence between obliquity and IRD abundance seen in the record (Figure S2c in Supporting Information S1). These results may indicate that obliquity paced the IRD peaks during MIS 13–15 after the obscure pacing period of the Mid-Pleistocene Transition (Starr et al., 2021), which may also relate to a non-linear response to orbital forcing (Starr et al., 2021; Willeit et al., 2019). We therefore suggest that either obliquity or mean annual insolation forcing (Patterson et al., 2014; Pollard & DeConto, 2009) may have played a role in driving additional mass loss of the WAIS during this interval.

## 6. Conclusions

This study provides sedimentological, mineralogical, and geochemical evidence for the evolving interaction between ocean-atmosphere forcing and WAIS instability in the South Pacific sector of the Southern Ocean from ~770 ka to present. We identify a series of intervals with elevated IRD content in core ANT34/A2-10, which appear to indicate persistent interglacial instability of the WAIS since ~770 ka. Over orbital timescales, increased IRD abundance during interglacials coincided with a shift in clay mineralogy in the fine fraction, which we interpret in terms of increased Ross Sea-sourced clay transported by the ACC. Together with evidence from previous studies for increased deepwater ventilation, poleward-shifted southern westerly winds, and a strengthened ACC during these intervals, our study supports a predominant control of ocean forcing on WAIS variability. Specifically, changes in the upwelling of CDW onto the shelves would have controlled basal melting, iceberg calving, and grounding line retreat.

In addition, Sr-Nd isotopes measured on bulk detrital sediments and the IRD samples (>250 μm) suggest a shift in provenance at around MIS 16, which we link to coupled atmosphere-ocean circulation changes in the region. We propose that changes in the intensity and position of the ASL and Ross Gyre led to a switch in iceberg trajectories and hence detrital provenance from predominantly Ross Sea sources (before MIS 16) to a combination of Ross, Amundsen, and Bellingshausen Sea sources (after MIS 16). However, categorically distinguishing between all potential provenance sources is difficult and other interpretations would be possible, so further work using multiple isotope systems and single-mineral $^{40}Ar/^{39}Ar$ and U/Pb evidence would be required to confirm this hypothesis. Interestingly, MIS 13 and MIS 15 were characterized by the highest IRD abundance and greatest IRD variability in the record, which may reflect a strong response of the WAIS to these changes in the ASL and Ross Gyre dynamics, while strong orbital forcing at this time and an influence from the weak intervening glacial period of MIS 14 could have driven additional ice loss.

## Conflict of Interest

The authors declare no conflicts of interest relevant to this study.

## Data Availability Statement

All iceberg-rafted debris content, clay mineralogy, and Sr-Nd isotope data presented in this study are available in the open science platform Zenodo (https://zenodo.org/) and can be accessed at https://doi.org/10.5281/zenodo.6787221.

**Acknowledgments**
The authors thank the 34th Chinese Antarctic Expedition cruise members and the Chinese Arctic and Antarctic Administration for retrieving the sediment core. The authors are also grateful to Julia Wellner, Reed Scherer, and three anonymous reviewers for their detailed and insightful comments, which significantly helped to improve this version of the manuscript, Branwen Williams for editorial handling, and Li Wu, Zhaojie Yu, and Xun Gong for their helpful suggestions. This work was supported by Impact and Response of Antarctic Seas to Climate Change (IRASCC2020-2022-01-03-02 and 02-03), Basic Scientific Fund for National Public Research Institutes of China (Grant Nos. 2019Q09, 2019S04, and 2017Y07), the National Natural Science Foundation of China (Grant Nos. 41976080 and 42076232), the Strategic Priority Research Program of the Chinese Academy of Sciences (Grant No. XDB42000000), and the Taishan Scholars Project Funding (Grant No. ts20190963). D. J. Wilson was supported by a Natural Environment Research Council independent research fellowship (NE/T011440/1).

## References

Adams, C. J., Pankhurst, R. J., Maas, R., & Millar, I. L. (2005). Nd and Sr isotopic signatures of metasedimentary rocks around the South Pacific margin and implications for their provenance. *Geological Society, London, Special Publications*, *246*(1), 113–141. https://doi.org/10.1144/gsl.sp.2005.246.01.04

Adusumilli, S., Fricker, H. A., Medley, B., Padman, L., & Siegfried, M. R. (2020). Interannual variations in meltwater input to the Southern Ocean from Antarctic ice shelves. *Nature Geoscience*, *13*(9), 616–620. https://doi.org/10.1038/s41561-020-0616-z

Anderson, J. B. (1999). *Antarctic marine geology*. Cambridge University Press.

Anderson, J. B., Brake, C. F., & Myers, N. C. (1984). Sedimentation on the Ross Sea continental shelf, Antarctica. *Marine Geology*, *57*(1–4), 295–333. https://doi.org/10.1016/0025-3227(84)90203-2

Anderson, R. F., Ali, S., Bradtmiller, L. I., Nielsen, S. H., Fleisher, M. Q., Anderson, B. E., & Burckle, L. H. (2009). Wind-driven upwelling in the Southern Ocean and the deglacial rise in atmospheric $CO_2$. *Science*, *323*(5920), 1443–1448. https://doi.org/10.1126/science.1167441

Andrews, J. T., & LeMasurier, W. (2021). Resolving the argument about volcanic bedrock under the West Antarctic Ice Sheet and implications for ice sheet stability and sea level change. *Earth and Planetary Science Letters*, *568*, 117035. https://doi.org/10.1016/j.epsl.2021.117035

Baines, P. G., & Fraedrich, K. (1988). Topographic effects on the mean tropospheric flow patterns around Antarctica. *Journal of the Atmospheric Sciences*, *46*(22), 3401–3415. https://doi.org/10.1175/1520-0469(1989)046

Basak, C., Frollje, H., Lamy, F., Gersonde, R., Benz, V., Anderson, R. F., et al. (2018). Breakup of last glacial deep stratification in the South Pacific. *Science*, *359*(6378), 900–904. https://doi.org/10.1126/science.aao2473

Bell, R. E. (2008). The role of subglacial water in ice-sheet mass balance. *Nature Geoscience*, *1*(5), 297–304. https://doi.org/10.1038/ngeo186

Bigg, G. R. (2020). The impact of icebergs of sub-Antarctic origin on Southern Ocean ice-rafted debris distributions. *Quaternary Science Reviews*, *232*, 106204. https://doi.org/10.1016/j.quascirev.2020.106204

Biscaye, P. E. (1965). Mineralogy and sedimentation of recent deep-sea clay in the Atlantic Ocean and adjacent seas and oceans. *The Geological Society of America Bulletin*, *76*(7), 803–832. https://doi.org/10.1130/0016-7606(1965)76[803:masord]2.0.co;2

Blakowski, M. A., Aciego, S. M., Delmonte, B., Baroni, C., Salvatore, M. C., & Sims, K. W. W. (2016). A Sr-Nd-Hf isotope characterization of dust source areas in Victoria Land and the McMurdo Sound sector of Antarctica. *Quaternary Science Reviews*, *141*, 26–37. https://doi.org/10.1016/j.quascirev.2016.03.023

Budillon, G., & Spezie, G. (2004). Thermohaline structure and variability in the Terra Nova Bay polynya, Ross Sea. *Antarctic Science*, *12*(4), 493–508. https://doi.org/10.1017/s0954102000000572

Caniupán, M., Lamy, F., Lange, C. B., Kaiser, J., Arz, H., Kilian, R., et al. (2011). Millennial-scale sea surface temperature and Patagonian Ice Sheet changes off southernmost Chile (53°S) over the past ~60 kyr. *Paleoceanography*, *26*(3), PA3221. https://doi.org/10.1029/2010pa002049

Ceccaroni, L., Frank, M., Frignani, M., Langone, L., Ravaioli, M., & Mangini, A. (1998). Late Quaternary fluctuations of biogenic component fluxes on the continental slope of the Ross Sea, Antarctica. *Journal of Marine Systems*, *17*(1–4), 515–525. https://doi.org/10.1016/s0924-7963(98)00061-x

Charles, C. D., Pahnke, K., Zahn, R., Mortyn, P. G., Ninnemann, U., & Hodell, D. A. (2010). Millennial scale evolution of the Southern Ocean chemical divide. *Quaternary Science Reviews*, *29*(3–4), 399–409. https://doi.org/10.1016/j.quascirev.2009.09.021

Civel-Mazens, M., Crosta, X., Cortese, G., Michel, E., Mazaud, A., Ther, O., et al. (2021). Antarctic Polar Front migrations in the Kerguelen Plateau region, Southern Ocean, over the past 360 kyrs. *Global and Planetary Change*, *202*, 103526. https://doi.org/10.1016/j.gloplacha.2021.103526

Conway, H., Hall, B. L., Denton, G. H., Gades, A. M., & Waddington, E. D. (1999). Past and future grounding-line retreat of the West Antarctic Ice Sheet. *Science*, *286*(5438), 280–283. https://doi.org/10.1126/science.286.5438.280

Das, I., Padman, L., Bell, R. E., Fricker, H. A., Tinto, K. J., Hulbe, C. L., et al. (2020). Multidecadal basal melt rates and structure of the Ross Ice Shelf, Antarctica, using airborne ice penetrating radar. *Journal of Geophysical Research: Earth Surface*, *125*(3), e2019JF005241. https://doi.org/10.1029/2019jf005241

Davis, P. E. D., Jenkins, A., Nicholls, K. W., Brennan, P. V., Abrahamsen, E. P., Heywood, K. J., et al. (2018). Variability in basal melting beneath Pine Island Ice Shelf on weekly to monthly timescales. *Journal of Geophysical Research: Oceans*, *123*(11), 8655–8669. https://doi.org/10.1029/2018jc014464

DeConto, R. M., & Pollard, D. (2016). Contribution of Antarctica to past and future sea-level rise. *Nature*, *531*(7596), 591–597. https://doi.org/10.1038/nature17145

Diekmann, B., Kuhn, G., Gersonde, R., & Mackensen, A. (2004). Middle Eocene to early Miocene environmental changes in the sub-Antarctic Southern Ocean: Evidence from biogenic and terrigenous depositional patterns at ODP Site 1090. *Global and Planetary Change*, *40*(3–4), 295–313. https://doi.org/10.1016/j.gloplacha.2003.09.001

Dotto, T. S., Naveira Garabato, A., Bacon, S., Tsamados, M., Holland, P. R., Hooley, J., et al. (2018). Variability of the Ross Gyre, Southern Ocean: Drivers and responses revealed by Satellite Altimetry. *Geophysical Research Letters*, *45*(12), 6195–6204. https://doi.org/10.1029/2018gl078607

Dotto, T. S., Naveira Garabato, A. C., Wåhlin, A. K., Bacon, S., Holland, P. R., Kimura, S., et al. (2020). Control of the Oceanic heat content of the Getz-Dotson Trough, Antarctica, by the Amundsen Sea Low. *Journal of Geophysical Research: Oceans*, *125*(8),e2020JC016113. https://doi.org/10.1029/2020jc016113

Ehrmann, W. (1998). Implications of late Eocene to early Miocene clay mineral assemblages in McMurdo Sound (Ross Sea, Antarctica) on paleoclimate and ice dynamics. *Palaeogeography, Palaeoclimatology, Palaeoecology*, *139*(3–4), 213–231. https://doi.org/10.1016/s0031-0182(97)00138-7

Ehrmann, W., Hillenbrand, C.-D., Smith, J. A., Graham, A. G. C., Kuhn, G., & Larter, R. D. (2011). Provenance changes between recent and glacial-time sediments in the Amundsen Sea embayment, West Antarctica: Clay mineral assemblage evidence. *Antarctic Science*, *23*(5), 471–486. https://doi.org/10.1017/s0954102011000320

Ehrmann, W., Setti, M., & Marinoni, L. (2005). Clay minerals in Cenozoic sediments off Cape Roberts (McMurdo Sound, Antarctica) reveal palaeoclimatic history. *Palaeogeography, Palaeoclimatology, Palaeoecology*, *229*(3), 187–211. https://doi.org/10.1016/j.palaeo.2005.06.022

England, M. R., Wagner, T. J. W., & Eisenman, I. (2020). Modeling the breakup of tabular icebergs. *Science Advances*, *6*(51), eabd1273. https://doi.org/10.1126/sciadv.abd1273

Esquevin, J. (1969). Influence de la composition chimique des illites sur leur cristallinité. *Bulletin du Centre de Recherches Pau-SNPA*, *3*, 147–153.

Farmer, G., Licht, K., Swope, R., & Andrews, J. (2006). Isotopic constraints on the provenance of fine-grained sediment in LGM tills from the Ross Embayment, Antarctica. *Earth and Planetary Science Letters*, *249*(1–2), 90–107. https://doi.org/10.1016/j.epsl.2006.06.044

Fogwill, C. J., Phipps, S. J., Turney, C. S. M., & Golledge, N. R. (2015). Sensitivity of the Southern Ocean to enhanced regional Antarctic ice sheet meltwater input. *Earth's Future*, *3*(10), 317–329. https://doi.org/10.1002/2015ef000306

Fudge, T. J., Steig, E. J., Markle, B. R., Schoenemann, S. W., Ding, Q., Taylor, K., et al. (2013). Onset of deglacial warming in West Antarctica driven by local orbital forcing. *Nature*, *500*(7463), 440–444. https://doi.org/10.1038/nature12376
Futa, K., & Le Masurier, W. E. (1983). Nd and Sr isotopic studies on Cenozoic mafic lavas from West Antarctica: Another source for continental alkali basalts. *Contributions to Mineralogy and Petrology*, *83*(1–2), 38–44. https://doi.org/10.1007/bf00373077
Gingele, F. X., De Deckker, P., & Hillenbrand, C.-D. (2001). Clay mineral distribution in surface sediments between Indonesia and NW Australia — Source and transport by ocean currents. *Marine Geology*, *179*(3–4), 135–146. https://doi.org/10.1016/s0025-3227(01)00194-3
Gingele, F. X., Müller, P. M., & Schneider, R. R. (1998). Orbital forcing of freshwater input in the Zaire fan area—Clay mineral evidence from the last 200 kyr. *Palaeogeography, Palaeoclimatology, Palaeoecology*, *138*(1–4), 17–26. https://doi.org/10.1016/s0031-0182(97)00121-1
Gladstone, R. M., Bigg, G. R., & Nicholls, K. W. (2001). Iceberg trajectory modeling and meltwater injection in the Southern Ocean. *Journal of Geophysical Research*, *106*(C9), 19903–19915. https://doi.org/10.1029/2000jc000347
Gohl, K., Wellner, J. S., Klaus, A., Bauersachs, T., Bohaty, S., Courtillat, M., et al. (2021). Expedition 379 summary. *Volume 379: Amundsen Sea West Antarctic Ice Sheet History*. https://doi.org/10.14379/iodp.proc.379.101.2021
Golledge, N. R., Keller, E. D., Gomez, N., Naughten, K. A., Bernales, J., Trusel, L. D., & Edwards, T. L. (2019). Global environmental consequences of twenty-first-century ice-sheet melt. *Nature*, *566*(7742), 65–72. https://doi.org/10.1038/s41586-019-0889-9
Gordon, A. L., Orsi, A. H., Muench, R., Huber, B. A., Zambianchi, E., & Visbeck, M. (2009). Western Ross Sea continental slope gravity currents. *Deep Sea Research Part II: Topical Studies in Oceanography*, *56*(13–14), 796–817. https://doi.org/10.1016/j.dsr2.2008.10.037
Grinsted, A., Moore, J. C., & Jevrejeva, S. (2004). Application of the cross wavelet transform and wavelet coherence to geophysical time series. *Nonlinear Processes in Geophysics*, *11*(5/6), 561–566. https://doi.org/10.5194/npg-11-561-2004
Hall, I. R., McCave, I. N., Shackleton, N. J., Weedon, G. P., & Harris, S. E. (2001). Intensified deep Pacific inflow and ventilation in Pleistocene glacial times. *Nature*, *412*(6849), 809–812. https://doi.org/10.1038/35090552
Hammer, Ø., & Harper, D. A. (2008). *Paleontological data analysis* (Online). John Wiley & Sons.
Hao, Q., Wang, L., Oldfield, F., & Guo, Z. (2015). Extra-long interglacial in Northern Hemisphere during MISs 15-13 arising from limited extent of Arctic ice sheets in glacial MIS 14. *Scientific Reports*, *5*(1), 12103. https://doi.org/10.1038/srep12103
Hart, S. R., Blusztajn, J., LeMasurier, W. E., & Rex, D. C. (1997). Hobbs Coast Cenozoic volcanism: Implications for the West Antarctic rift system. *Chemical Geology*, *139*(1–4), 223–248. https://doi.org/10.1016/s0009-2541(97)00037-5
Hattermann, T., Nicholls, K. W., Hellmer, H. H., Davis, P. E. D., Janout, M. A., Osterhus, S., et al. (2021). Observed interannual changes beneath Filchner-Ronne Ice Shelf linked to large-scale atmospheric circulation. *Nature Communications*, *12*(1), 2961. https://doi.org/10.1038/s41467-021-23131-x
Heath, S., Hall, B. L., Denton, G. H., Henderson, G. M., & Hendy, C. H. (2022). Ice-sheet expansion from the Ross Sea into McMurdo Sound, Antarctica, during the last two glaciations. *Quaternary Science Reviews*, *278*, 107379. https://doi.org/10.1016/j.quascirev.2022.107379
Hillenbrand, C.-D. (2000). *Glaciomarine sedimentation on the continental margins of the Amundsen and Bellingshausen Seas, West Antarctica – Indications for paleoenvironmental changes during the Quaternary climatic cycles*. Reports on Polar Research. Alfred Wegener Institute for Polar and Marine Research.
Hillenbrand, C. D., Crowhurst, S. J., Williams, M., Hodell, D. A., McCave, I. N., Ehrmann, W., et al. (2021). New insights from multi-proxy data from the West Antarctic continental rise: Implications for dating and interpreting Late Quaternary palaeoenvironmental records. *Quaternary Science Reviews*, *257*, 106842. https://doi.org/10.1016/j.quascirev.2021.106842
Hillenbrand, C.-D., & Ehrmann, W. (2005). Late Neogene to Quaternary environmental changes in the Antarctic Peninsula region: Evidence from drift sediments. *Global and Planetary Change*, *45*(1–3), 165–191. https://doi.org/10.1016/j.gloplacha.2004.09.006
Hillenbrand, C.-D., Fütterer, D., Grobe, H., & Frederichs, T. (2002). No evidence for a Pleistocene collapse of the West Antarctic Ice Sheet from continental margin sediments recovered in the Amundsen Sea. *Geo-Marine Letters*, *22*(2), 51–59. https://doi.org/10.1007/s00367-002-0097-7
Hillenbrand, C.-D., Grobe, H., Diekmann, B., Kuhn, G., & Fütterer, D. K. (2003). Distribution of clay minerals and proxies for productivity in surface sediments of the Bellingshausen and Amundsen seas (West Antarctica) – Relation to modern environmental conditions. *Marine Geology*, *193*(3–4), 253–271. https://doi.org/10.1016/s0025-3227(02)00659-x
Hillenbrand, C. D., Kuhn, G., & Frederichs, T. (2009). Record of a Mid-Pleistocene depositional anomaly in West Antarctic continental margin sediments: An indicator for ice-sheet collapse? *Quaternary Science Reviews*, *28*(13–14), 1147–1159. https://doi.org/10.1016/j.quascirev.2008.12.010
Hillenbrand, C.-D., Melles, M., Kuhn, G., & Larter, R. D. (2012). Marine geological constraints for the grounding-line position of the Antarctic Ice Sheet on the southern Weddell Sea shelf at the last glacial maximum. *Quaternary Science Reviews*, *32*, 25–47. https://doi.org/10.1016/j.quascirev.2011.11.017
Hillenbrand, C. D., Smith, J. A., Hodell, D. A., Greaves, M., Poole, C. R., Kender, S., et al. (2017). West Antarctic Ice Sheet retreat driven by Holocene warm water incursions. *Nature*, *547*(7661), 43–48. https://doi.org/10.1038/nature22995
Hillenbrand, E. (2001). Distribution of clay minerals in drift sediments on the continental rise west of the Antarctic peninsula, ODP Leg 178, Sites 1095 and 1096. *Proceedings of the Ocean Drilling Program – Scientific Results*, *178*, 1–29.
Hiscock, M. R. (2004). *The regulation of primary productivity in the Southern Ocean* (PhD thesis). Duke University.
Ho, S. L., Mollenhauer, G., Lamy, F., Martinez-Garcia, A., Mohtadi, M., Gersonde, R., et al. (2012). Sea surface temperature variability in the Pacific sector of the Southern Ocean over the past 700 kyr. *Paleoceanography*, *27*(4). https://doi.org/10.1029/2012pa002317
Hodell, D. A., Venz, K. A., Charles, C. D., & Ninnemann, U. S. (2003). Pleistocene vertical carbon isotope and carbonate gradients in the South Atlantic sector of the Southern Ocean. *Geochemistry, Geophysics, Geosystems*, *4*(1), 1–19. https://doi.org/10.1029/2002gc000367
Hofmann, E. E., Klinck, J. M., & Dinniman, M. S. (2012). Sensitivity of Circumpolar Deep Water transport and Ice Shelf basal melt along the West Antarctic Peninsula to changes in the Winds. *Journal of Climate*, *25*(14), 4799–4816. https://doi.org/10.1175/jcli-d-11-00307.1
Holland, P. R., Bracegirdle, T. J., Dutrieux, P., Jenkins, A., & Steig, E. J. (2019). West Antarctic ice loss influenced by internal climate variability and anthropogenic forcing. *Nature Geoscience*, *12*(9), 718–724. https://doi.org/10.1038/s41561-019-0420-9
Hosking, J. S., Orr, A., Bracegirdle, T. J., & Turner, J. (2016). Future circulation changes off West Antarctica: Sensitivity of the Amundsen Sea Low to projected anthropogenic forcing. *Geophysical Research Letters*, *43*(1), 367–376. https://doi.org/10.1002/2015gl067143
Hosking, J. S., Orr, A., Marshall, G. J., Turner, J., & Phillips, T. (2013). The influence of the Amundsen–Bellingshausen Seas low on the climate of West Antarctica and its representation in coupled climate model simulations. *Journal of Climate*, *26*(17), 6633–6648. https://doi.org/10.1175/jcli-d-12-00813.1
Jacobs, S. S., & Comiso, J. C. (1997). Climate variability in the Amundsen and Bellingshausen Seas. *Journal of Climate*, *10*(4), 697–709. https://doi.org/10.1175/1520-0442(1997)0102.0.CO;2
Jacobs, S. S., Hellmer, H. H., & Jenkins, A. (1996). Antarctic Ice Sheet melting in the southeast Pacific. *Geophysical Research Letters*, *23*(9), 957–960. https://doi.org/10.1029/96gl00723

Jacobs, S. S., Helmer, H. H., Doake, C. S. M., Jenkins, A., & Frolich, R. M. (1992). Melting of ice shelves and the mass balance of Antarctica. *Journal of Glaciology*, *38*(130), 375–387. https://doi.org/10.3189/s0022143000002252

Jacobs, S. S., Jenkins, A., Giulivi, C. F., & Dutrieux, P. (2011). Stronger ocean circulation and increased melting under Pine Island Glacier ice shelf. *Nature Geoscience*, *4*(8), 519–523. https://doi.org/10.1038/ngeo1188

Jacobs, S. S., Jenkins, A., Hellmer, H., Giulivi, C., Nitsche, F., Huber, B., & Guerrero, R. (2012). The Amundsen Sea and the Antarctic Ice Sheet. *Oceanography*, *25*(3), 154–163. https://doi.org/10.5670/oceanog.2012.90

Jacobsen, S. B., & Wasserburg, G. J. (1980). Sm-Nd isotopic evolution of chondrites. *Earth and Planetary Science Letters*, *50*(1), 139–155. https://doi.org/10.1016/0012-821x(80)90125-9

Jones, R. S., Gudmundsson, G. H., Mackintosh, A. N., McCormack, F. S., & Whitmore, R. J. (2021). Ocean-driven and topography-controlled nonlinear glacier retreat during the Holocene: Southwestern Ross Sea, Antarctica. *Geophysical Research Letters*, *48*(5), e2020GL091454. https://doi.org/10.1029/2020gl091454

Joughin, I., & Alley, R. B. (2011). Stability of the West Antarctic Ice Sheet in a warming world. *Nature Geoscience*, *4*(8), 506–513. https://doi.org/10.1038/ngeo1194

Joughin, I., Smith, B. E., & Medley, B. (2014). Marine ice sheet collapse potentially under way for the Thwaites Glacier Basin, West Antarctica. *Science*, *344*(6185), 735–738. https://doi.org/10.1126/science.1249055

Jouzel, J., Masson-Delmotte, V., Cattani, O., Dreyfus, G., Falourd, S., Hoffmann, G., et al. (2007). Orbital and millennial Antarctic climate variability over the past 800,000 years. *Science*, *317*(5839), 793–796. https://doi.org/10.1126/science.1141038

Jung, J., Ko, Y., Lee, J., Yang, K., Park, Y. K., Kim, S., et al. (2021). Multibeam bathymetry and distribution of clay minerals on surface sediments of a Small Bay in Terra Nova Bay, Antarctica. *Minerals*, *11*(1), 72. https://doi.org/10.3390/min11010072

Kanfoush, S. L., Hodell, D. A., Charles, C. D., Guilderson, T. P., Mortyn, P. G., & Ninnemann, U. S. (2000). Millennial-scale instability of the Antarctic ice sheet during the last glaciation. *Science*, *288*(5472), 1815–1818. https://doi.org/10.1126/science.288.5472.1815

Kim, T. W., Yang, H. W., Dutrieux, P., Wåhlin, A. K., Jenkins, A., Kim, Y. G., et al. (2021). Interannual variation of Modified Circumpolar Deep Water in the Dotson-Getz trough, West Antarctica. *Journal of Geophysical Research: Oceans*, *126*(12), e2021JC017491. https://doi.org/10.1029/2021jc017491

Konfirst, M. A., Scherer, R. P., Hillenbrand, C.-D., & Kuhn, G. (2012). A marine diatom record from the Amundsen Sea — Insights into oceanographic and climatic response to the Mid-Pleistocene transition in the West Antarctic sector of the Southern Ocean. *Marine Micropaleontology*, *92–93*, 40–51. https://doi.org/10.1016/j.marmicro.2012.05.001

Korhonen, F. J., Saito, S., Brown, M., Siddoway, C. S., & Day, J. M. D. (2010). Multiple generations of granite in the Fosdick Mountains, Marie Byrd Land, West Antarctica: Implications for polyphase intracrustal differentiation in a continental margin setting. *Journal of Petrology*, *51*(3), 627–670. https://doi.org/10.1093/petrology/egp093

Laskar, J., Robutel, P., Joutel, F., Gastineau, M., Correia, A. C. M., & Levrard, B. (2004). A long-term numerical solution for the insolation quantities of the Earth. *Astronomy & Astrophysics*, *428*(1), 261–285. https://doi.org/10.1051/0004-6361:20041335

Lear, C. H., Rosenthal, Y., Coxall, H. K., & Wilson, P. A. (2004). Late Eocene to early Miocene ice sheet dynamics and the global carbon cycle. *Paleoceanography*, *19*(4), PA4015. https://doi.org/10.1029/2004pa001039

Levy, R. H., Meyers, S. R., Naish, T. R., Golledge, N. R., McKay, R. M., Crampton, J. S., et al. (2019). Antarctic ice-sheet sensitivity to obliquity forcing enhanced through ocean connections. *Nature Geoscience*, *12*(2), 132–137. https://doi.org/10.1038/s41561-018-0284-4

Li, J., Tang, S. H., Zhu, X. K., & Pan, C. X. (2017). Production and certification of the reference material GSB 04-3258-2015 as a $^{143}Nd/^{144}Nd$ isotope ratio reference. *Geostandards and Geoanalytical Research*, *41*(2), 255–262. https://doi.org/10.1111/ggr.12151

Li, M. S., Hinnov, L., & Kump, L. (2019). Acycle: Time-series analysis software for paleoclimate research and education. *Computers & Geosciences*, *127*, 12–22. https://doi.org/10.1016/j.cageo.2019.02.011

Lindgren, A., Hugelius, G., & Kuhry, P. (2018). Extensive loss of past permafrost carbon but a net accumulation into present-day soils. *Nature*, *560*(7717), 219–222. https://doi.org/10.1038/s41586-018-0371-0

Lisiecki, L. E., & Raymo, M. E. (2005). A Pliocene-Pleistocene stack of 57 globally distributed benthic $\delta^{18}O$ records. *Paleoceanography*, *20*(1), PA1003. https://doi.org/10.1029/2004pa001071

Liu, Y., Moore, J. C., Cheng, X., Gladstone, R. M., Bassis, J. N., Liu, H., et al. (2015). Ocean-driven thinning enhances iceberg calving and retreat of Antarctic ice shelves. *Proceedings of the National Academy of Sciences of the United States of America*, *112*(11), 3263–3268. https://doi.org/10.1073/pnas.1415137112

Loutre, M.-F., Paillard, D., Vimeux, F., & Cortijo, E. (2004). Does mean annual insolation have the potential to change the climate? *Earth and Planetary Science Letters*, *221*(1–4), 1–14. https://doi.org/10.1016/s0012-821x(04)00108-6

Lowe, A., & Anderson, J. (2002). Reconstruction of the West Antarctic Ice Sheet in Pine Island Bay during the last glacial maximum and its subsequent retreat history. *Quaternary Science Reviews*, *21*(16–17), 1879–1897. https://doi.org/10.1016/s0277-3791(02)00006-9

Marschalek, J. W., Zurli, L., Talarico, F., van de Flierdt, T., Vermeesch, P., Carter, A., et al. (2021). A large West Antarctic Ice Sheet explains early Neogene sea-level amplitude. *Nature*, *600*(7889), 450–455. https://doi.org/10.1038/s41586-021-04148-0

McCarron, J. J., & Smellie, J. L. (1998). Tectonic implications of fore-arc magmatism and generation of high-magnesian andesites: Alexander Island, Antarctica. *Journal of the Geological Society*, *155*(2), 269–280. https://doi.org/10.1144/gsjgs.155.2.0269

Menviel, L., Timmermann, A., Timm, O. E., & Mouchet, A. (2010). Climate and biogeochemical response to a rapid melting of the West Antarctic Ice Sheet during interglacials and implications for future climate. *Paleoceanography*, *25*(4), PA4231. https://doi.org/10.1029/2009pa001892

Nakayama, Y., Menemenlis, D., Zhang, H., Schodlok, M., & Rignot, E. (2018). Origin of Circumpolar Deep Water intruding onto the Amundsen and Bellingshausen Sea continental shelves. *Nature Communications*, *9*(1), 3403. https://doi.org/10.1038/s41467-018-05813-1

Nerem, R. S., Beckley, B. D., Fasullo, J. T., Hamlington, B. D., Masters, D., & Mitchum, G. T. (2018). Climate-change-driven accelerated sea-level rise detected in the altimeter era. *Proceedings of the National Academy of Sciences of the United States of America*, *115*(9), 2022–2025. https://doi.org/10.1073/pnas.1717312115

Nielsen, S. H. H., Hodell, D. A., Kamenov, G., Guilderson, T., & Perfit, M. R. (2007). Origin and significance of ice-rafted detritus in the Atlantic sector of the Southern Ocean. *Geochemistry, Geophysics, Geosystems*, *8*(12), Q12005. https://doi.org/10.1029/2007gc001618

O'Connor, G. K., Steig, E. J., & Hakim, G. J. (2021). Strengthening Southern Hemisphere westerlies and Amundsen Sea Low deepening over the 20th century revealed by proxy-data assimilation. *Geophysical Research Letters*, *48*(24), e2021GL095999. https://doi.org/10.1029/2021gl095999

Orsi, A. H., Johnson, G. C., & Bullister, J. L. (1999). Circulation, mixing, and production of Antarctic bottom water. *Progress in Oceanography*, *43*(1), 55–109. https://doi.org/10.1016/s0079-6611(99)00004-x

Orsi, A. H., Whitworth, T., & Nowlin, W. D. (1995). On the meridional extent and fronts of the Antarctic Circumpolar Current. *Deep Sea Research Part I: Oceanographic Research Papers*, *42*(5), 641–673. https://doi.org/10.1016/0967-0637(95)00021-w

Orsi, A. H., & Wiederwohl, C. L. (2009). A recount of Ross Sea waters. *Deep Sea Research Part II: Topical Studies in Oceanography*, *56*(13–14), 778–795. https://doi.org/10.1016/j.dsr2.2008.10.033

Pankhurst, R. J., Millar, I. L., Grunow, A. M., & Storey, B. C. (1993). The pre-Cenozoic magmatic history of the Thurston Island crustal block, West Antarctica. *Journal of Geophysical Research*, *98*(B7), 11835–11849. https://doi.org/10.1029/93jb01157

Pant, N. C., Biswas, P., Shrivastava, P. K., Bhattacharya, S., Verma, K., & Pandey, M. (2013). *Provenance of Pleistocene sediments from Site U1359 of the Wilkes Land IODP Leg 318 – Evidence for multiple sourcing from the East Antarctic Craton and Ross Orogen* (Vol. 381). Geological Society.

Patterson, M. O., McKay, R., Naish, T., Escutia, C., Jimenez-Espejo, F. J., Raymo, M. E., et al. (2014). Orbital forcing of the East Antarctic ice sheet during the Pliocene and Early Pleistocene. *Nature Geoscience*, *7*(11), 841–847. https://doi.org/10.1038/ngeo2273

Pattyn, F., & Morlighem, M. (2020). The uncertain future of the Antarctic Ice Sheet. *Science*, *367*(6484), 1331–1335. https://doi.org/10.1126/science.aaz5487

Peck, V. L., Allen, C. S., Kender, S., McClymont, E. L., & Hodgson, D. A. (2015). Oceanographic variability on the West Antarctic Peninsula during the Holocene and the influence of upper Circumpolar Deep Water. *Quaternary Science Reviews*, *119*, 54–65. https://doi.org/10.1016/j.quascirev.2015.04.002

Perez, L. F., Martos, Y. M., Garcia, M., Weber, M. E., Raymo, M. E., Williams, T., et al. (2021). Miocene to present oceanographic variability in the Scotia Sea and Antarctic ice sheets dynamics: Insight from revised seismic-stratigraphy following IODP Expedition 382. *Earth and Planetary Science Letters*, *553*, 116657. https://doi.org/10.1016/j.epsl.2020.1166570012–821X

Petschick, R., Kuhn, G., & Gingele, F. (1996). Clay mineral distribution in surface sediments of the South Atlantic: Sources, transport, and relation to oceanography. *Marine Geology*, *130*(3–4), 203–229. https://doi.org/10.1016/0025-3227(95)00148-4

Pollard, D., & DeConto, R. M. (2009). Modelling West Antarctic Ice Sheet growth and collapse through the past five million years. *Nature*, *458*(7236), 329–332. https://doi.org/10.1038/nature07809

Pollard, D., DeConto, R. M., & Alley, R. B. (2015). Potential Antarctic Ice Sheet retreat driven by hydrofracturing and ice cliff failure. *Earth and Planetary Science Letters*, *412*, 112–121. https://doi.org/10.1016/j.epsl.2014.12.035

Presti, M., Barbara, L., Denis, D., Schmidt, S., De Santis, L., & Crosta, X. (2011). Sediment delivery and depositional patterns off Adélie Land (East Antarctica) in relation to late Quaternary climatic cycles. *Marine Geology*, *284*(1–4), 96–113. https://doi.org/10.1016/j.margeo.2011.03.012

Pritchard, H. D., Ligtenberg, S. R., Fricker, H. A., Vaughan, D. G., van den Broeke, M. R., & Padman, L. (2012). Antarctic ice-sheet loss driven by basal melting of ice shelves. *Nature*, *484*(7395), 502–505. https://doi.org/10.1038/nature10968

Rickli, J., Gutjahr, M., Vance, D., Fischer-Gödde, M., Hillenbrand, C.-D., & Kuhn, G. (2014). Neodymium and hafnium boundary contributions to seawater along the West Antarctic continental margin. *Earth and Planetary Science Letters*, *394*, 99–110. https://doi.org/10.1016/j.epsl.2014.03.008

Rignot, E., Jacobs, S., Mouginot, J., & Scheuchl, B. (2013). Ice-shelf melting around Antarctica. *Science*, *341*(6143), 266–270. https://doi.org/10.1126/science.1235798

Rignot, E., & Jacobs, S. S. (2002). Rapid bottom melting widespread near Antarctic Ice Sheet grounding lines. *Science*, *296*(5575), 2020–2023. https://doi.org/10.1126/science.1070942

Rignot, E., Mouginot, J., Morlighem, M., Seroussi, H., & Scheuchl, B. (2014). Widespread, rapid grounding line retreat of Pine Island, Thwaites, Smith, and Kohler glaciers, West Antarctica, from 1992 to 2011. *Geophysical Research Letters*, *41*(10), 3502–3509. https://doi.org/10.1002/2014gl060140

Rignot, E., Mouginot, J., Scheuchl, B., van den Broeke, M., van Wessem, M. J., & Morlighem, M. (2019). Four decades of Antarctic Ice Sheet mass balance from 1979–2017. *Proceedings of the National Academy of Sciences of the United States of America*, *116*(4), 1095–1103. https://doi.org/10.1073/pnas.1812883116

Riley, T. R., Leat, P. T., Pankhurst, R. J., & Harris, C. (2001). Origins of large volume Rhyolitic volcanism in the Antarctic Peninsula and Patagonia by crustal melting. *Journal of Petrology*, *42*(6), 1043–1065. https://doi.org/10.1093/petrology/42.6.1043

Ryan, C. (2007). *Mesozoic to Cenozoic igneous rocks from Northwestern Graham Land: Constraints on the tectonomagmatic evolution of the Antarctic Peninsula*. University of Brighton.

Schmidtko, S., Heywood, K. J., Thompson, A. F., & Aoki, S. (2014). Multidecadal warming of Antarctic waters. *Science*, *346*(6214), 1227–1231. https://doi.org/10.1126/science.1256117

Setti, M., Marinoni, L., & López-Galindo, A. (2004). Mineralogical and geochemical characteristics (major, minor, trace elements and REE) of detrital and authigenic clay minerals in a Cenozoic sequence from Ross Sea, Antarctica. *Clay Minerals*, *39*(4), 405–421. https://doi.org/10.1180/000985503540143

Shepherd, A., Fricker, H. A., & Farrell, S. L. (2018). Trends and connections across the Antarctic cryosphere. *Nature*, *558*(7709), 223–232. https://doi.org/10.1038/s41586-018-0171-6

Shepherd, A., Ivins, E., Rignot, E., Smith, B., Van Den Broeke, M., Velicogna, I., & Nowicki, S. E. (2018). Mass balance of the Antarctic Ice Sheet from 1992 to 2017. *Nature*, *558*(7709), 219–222. https://doi.org/10.1038/s41586-018-0179-y

Silva, T. A. M., Bigg, G. R., & Nicholls, K. W. (2006). Contribution of giant icebergs to the Southern Ocean freshwater flux. *Journal of Geophysical Research*, *111*(C3), C03004. https://doi.org/10.1029/2004jc002843

Simões Pereira, P., van de Flierdt, T., Hemming, S. R., Frederichs, T., Hammond, S. J., Brachfeld, S., et al. (2020). The geochemical and mineralogical fingerprint of West Antarctica's weak underbelly: Pine Island and Thwaites glaciers. *Chemical Geology*, *550*, 119649. https://doi.org/10.1016/j.chemgeo.2020.119649

Simões Pereira, P., van de Flierdt, T., Hemming, S. R., Hammond, S. J., Kuhn, G., Brachfeld, S., et al. (2018). Geochemical fingerprints of glacially eroded bedrock from West Antarctica: Detrital thermochronology, radiogenic isotope systematics and trace element geochemistry in Late Holocene glacial-marine sediments. *Earth-Science Reviews*, *182*, 204–232. https://doi.org/10.1016/j.earscirev.2018.04.011

Smith, J. A., Graham, A. G. C., Post, A. L., Hillenbrand, C. D., Bart, P. J., & Powell, R. D. (2019). The marine geological imprint of Antarctic ice shelves. *Nature Communications*, *10*(1), 5635. https://doi.org/10.1038/s41467-019-13496-5

Smith, K. L. (2011). Free-drifting icebergs in the Southern Ocean: An overview. *Deep Sea Research Part II: Topical Studies in Oceanography*, *58*(11–12), 1277–1284. https://doi.org/10.1016/j.dsr2.2010.11.003

Smith, W. O., Shields, A. R., Peloquin, J. A., Catalano, G., Tozzi, S., Dinniman, M. S., & Asper, V. A. (2006). Interannual variations in nutrients, net community production, and biogeochemical cycles in the Ross Sea. *Deep Sea Research Part II: Topical Studies in Oceanography*, *53*(8–10), 815–833. https://doi.org/10.1016/j.dsr2.2006.02.014

Starr, A., Hall, I. R., Barker, S., Rackow, T., Zhang, X., Hemming, S. R., et al. (2021). Antarctic icebergs reorganize ocean circulation during Pleistocene glacials. *Nature*, *589*(7841), 236–241. https://doi.org/10.1038/s41586-020-03094-7

Steig, E. J., Ding, Q., Battisti, D. S., & Jenkins, A. (2012). Tropical forcing of Circumpolar Deep Water Inflow and outlet glacier thinning in the Amundsen Sea embayment, West Antarctica. *Annals of Glaciology*, *53*(60), 19–28. https://doi.org/10.3189/2012AoG60A110

Sutter, J., Fischer, H., Grosfeld, K., Karlsson, N. B., Kleiner, T., Van Liefferinge, B., & Eisen, O. (2019). Modelling the Antarctic Ice Sheet across the Mid-Pleistocene transition – Implications for Oldest Ice. *The Cryosphere*, *13*(7), 2023–2041. https://doi.org/10.5194/tc-13-2023-2019

Tanaka, T., Togashi, S., Kamioka, H., Amakawa, H., Kagami, H., Hamamoto, T., et al. (2000). JNdi-1: A neodymium isotopic reference in consistency with LaJolla neodymium. *Chemical Geology*, *168*(3–4), 279–281. https://doi.org/10.1016/s0009-2541(00)00198-4

Tang, Z., Li, T., Xiong, Z., Dang, H., Guo, J., & Cheng, F. (2022). Covariation of Deep Antarctic Pacific Oxygenation and atmospheric $CO_2$ during the last 770 kyr. *Lithosphere*, *2022*(Special 9), 1835176. https://doi.org/10.2113/2022/1835176

Teitler, L., Warnke, D. A., Venz, K. A., Hodell, D. A., Becquey, S., Gersonde, R., & Teitler, W. (2010). Determination of Antarctic Ice Sheet stability over the last ~500 ka through a study of iceberg-rafted debris. *Paleoceanography*, *25*(1), PA1202. https://doi.org/10.1029/2008pa001691

Thoma, M., Jenkins, A., Holland, D., & Jacobs, S. (2008). Modelling Circumpolar Deep Water intrusions on the Amundsen Sea continental shelf, Antarctica. *Geophysical Research Letters*, *35*(18), L18602. https://doi.org/10.1029/2008gl034939

Tinto, K. J., Padman, L., Siddoway, C. S., Springer, S. R., Fricker, H. A., Das, I., et al. (2019). Ross Ice Shelf response to climate driven by the tectonic imprint on seafloor bathymetry. *Nature Geoscience*, *12*(6), 441–449. https://doi.org/10.1038/s41561-019-0370-2

Toggweiler, J. R., Russell, J. L. & Carson, S. R. (2006). Midlatitude westerlies, atmospheric CO2, and climate change during the ice ages. *Paleoceanography*. *21*(2). https://doi.org/10.1029/2005pa001154

Totten, R. L., Fonseca, A. N. R., Wellner, J. S., Munoz, Y. P., Anderson, J. B., Tobin, T. S., & Lehrmann, A. A. (2022). Oceanographic and climatic influences on Trooz glacier, Antarctica during the Holocene. *Quaternary Science Reviews*, *276*, 107279. https://doi.org/10.1016/j.quascirev.2021.107279

Tournadre, J., Bouhier, N., Girard-Ardhuin, F., & Rémy, F. (2015). Antarctic icebergs distributions 1992–2014. *Journal of Geophysical Research: Oceans*, *121*(1), 327–349. https://doi.org/10.1002/2015jc011178

Toyos, M. H., Lamy, F., Lange, C. B., Lembke-Jene, L., Saavedra-Pellitero, M., Esper, O., & Arz, H. W. (2020). Antarctic Circumpolar Current dynamics at the Pacific entrance to the Drake Passage over the past 1.3 million years. *Paleoceanography and Paleoclimatology*, *35*(7), e2019PA003773. https://doi.org/10.1029/2019pa003773

Turner, J., Phillips, T., Hosking, J. S., Marshall, G. J., & Orr, A. (2013). The Amundsen Sea Low. *International Journal of Climatology*, *33*(7), 1818–1829. https://doi.org/10.1002/joc.3558

Turney, C. S. M., Fogwill, C. J., Golledge, N. R., McKay, N. P., van Sebille, E., Jones, R. T., et al. (2020). Early Last Interglacial ocean warming drove substantial ice mass loss from Antarctica. *Proceedings of the National Academy of Sciences of the United States of America*, *117*(8), 3996–4006. https://doi.org/10.1073/pnas.1902469117

Uenzelmann-Neben, G., & Gohl, K. (2012). Amundsen Sea sediment drifts: Archives of modifications in oceanographic and climatic conditions. *Marine Geology*, *299–302*, 51–62. https://doi.org/10.1016/j.margeo.2011.12.007

Ullermann, J., Lamy, F., Ninnemann, U., Lembke-Jene, L., Gersonde, R., & Tiedemann, R. (2016). Pacific-Atlantic Circumpolar Deep Water coupling during the last 500 ka. *Paleoceanography*, *31*(6), 639–650. https://doi.org/10.1002/2016pa002932

Wadham, J. L., Hawkings, J. R., Tarasov, L., Gregoire, L. J., Spencer, R. G. M., Gutjahr, M., et al. (2019). Ice sheets matter for the global carbon cycle. *Nature Communications*, *10*(1), 3567. https://doi.org/10.1038/s41467-019-11394-4

Wahlin, A. K., Graham, A. G. C., Hogan, K. A., Queste, B. Y., Boehme, L., Larter, R. D., et al. (2021). Pathways and modification of warm water flowing beneath Thwaites Ice Shelf, West Antarctica. *Science Advances*, *7*(15), eabd7254. https://doi.org/10.1126/sciadv.abd7254

Walker, D. P., Brandon, M. A., Jenkins, A., Allen, J. T., Dowdeswell, J. A., & Evans, J. (2007). Oceanic heat transport onto the Amundsen Sea shelf through a submarine glacial trough. *Geophysical Research Letters*, *34*(2), L02602. https://doi.org/10.1029/2006gl028154

Wan, S., Clift, P. D., Zhao, D. B., Hovius, N., Munhoven, G., France-Lanord, C., et al. (2017). Enhanced silicate weathering of tropical shelf sediments exposed during glacial lowstands: A sink for atmospheric $CO_2$. *Geochimica et Cosmochimica Acta*, *200*, 123–144. https://doi.org/10.1016/j.gca.2016.12.010

Wan, S., Li, A., Clift, P. D., & Jiang, H. (2006). Development of the East Asian summer monsoon: Evidence from the sediment record in the South China Sea since 8.5 Ma. *Palaeogeography, Palaeoclimatology, Palaeoecology*, *241*(1), 139–159. https://doi.org/10.1016/j.palaeo.2006.06.013

Wan, S., Li, A., Clift, P. D., & Stuut, J.-B. W. (2007). Development of the East Asian monsoon: Mineralogical and sedimentologic records in the northern South China Sea since 20 Ma. *Palaeogeography, Palaeoclimatology, Palaeoecology*, *254*(3–4), 561–582. https://doi.org/10.1016/j.palaeo.2007.07.009

Wan, S., Tian, J., Steinke, S., Li, A., & Li, T. (2010). Evolution and variability of the East Asian summer monsoon during the Pliocene: Evidence from clay mineral records of the South China Sea. *Palaeogeography, Palaeoclimatology, Palaeoecology*, *293*(1–2), 237–247. https://doi.org/10.1016/j.palaeo.2010.05.025

Wang, S., Liu, J., Cheng, X., Kerzenmacher, T., & Braesicke, P. (2020). Is enhanced Predictability of the Amundsen Sea Low in Subseasonal to Seasonal Hindcasts linked to Stratosphere-Troposphere Coupling? *Geophysical Research Letters*, *47*(18), e2020GL089700. https://doi.org/10.1029/2020gl089700

Watkins, N. D., Keany, J., Ledbetter, M. T., & Huang, T. C. (1974). Antarctic glacial history from analyses of ice-rafted deposits in marine sediments: New model and initial tests. *Science*, *186*(4163), 533–536. https://doi.org/10.1126/science.186.4163.533

Weber, M. E., Clark, P. U., Kuhn, G., Timmermann, A., Sprenk, D., Gladstone, R., et al. (2014). Millennial-scale variability in Antarctic ice-sheet discharge during the last deglaciation. *Nature*, *510*(7503), 134–138. https://doi.org/10.1038/nature13397

Weber, M. E., Golledge, N. R., Fogwill, C. J., Turney, C. S. M., & Thomas, Z. A. (2021). Decadal-scale onset and termination of Antarctic ice-mass loss during the last deglaciation. *Nature Communications*, *12*(1), 6683. https://doi.org/10.1038/s41467-021-27053-6

Weis, D., Kieffer, B., Maerschalk, C., Barling, J., de Jong, J., Williams, G. A., et al. (2006). High-precision isotopic characterization of USGS reference materials by TIMS and MC-ICP-MS. *Geochemistry, Geophysics, Geosystems*, *7*(8), Q08006. https://doi.org/10.1029/2006gc001283

Willeit, M., Ganopolski, A., Calov, R., & Brovkin, V. (2019). Mid-Pleistocene transition in glacial cycles explained by declining $CO_2$ and regolith removal. *Science Advances*, *5*(4), eaav7337. https://doi.org/10.1126/sciadv.aav7337

Wilson, D. J., Bertram, R. A., Needham, E. F., van de Flierdt, T., Welsh, K. J., McKay, R. M., et al. (2018). Ice loss from the East Antarctic Ice Sheet during late Pleistocene interglacials. *Nature*, *561*(7723), 383–386. https://doi.org/10.1038/s41586-018-0501-8

Wolff, E. W., Barbante, C., Becagli, S., Bigler, M., Boutron, C., Castellano, E., et al. (2010). Changes in environment over the last 800,000 years from chemical analysis of the EPICA Dome C ice core. *Quaternary Science Reviews*, *29*(1–2), 285–295. https://doi.org/10.1016/j.quascirev.2009.06.013

Wu, L., Wang, R., Xiao, W., Ge, S., Chen, Z., & Krijgsman, W. (2017). Productivity-climate coupling recorded in Pleistocene sediments off Prydz Bay (East Antarctica). *Palaeogeography, Palaeoclimatology, Palaeoecology*, *485*, 260–270. https://doi.org/10.1016/j.palaeo.2017.06.018

Wu, L., Wang, R., Xiao, W., Krijgsman, W., Li, Q., Ge, S., & Ma, T. (2018). Late Quaternary deep stratification-climate coupling in the Southern Ocean: Implications for changes in abyssal carbon storage. *Geochemistry, Geophysics, Geosystems*, *19*(2), 379–395. https://doi.org/10.1002/2017gc007250

Wu, L., Wilson, D. J., Wang, R., Passchier, S., Krijgsman, W., Yu, X., et al. (2021). Late Quaternary dynamics of the Lambert Glacier-Amery Ice Shelf system, East Antarctica. *Quaternary Science Reviews*, *252*, 106738. https://doi.org/10.1016/j.quascirev.2020.106738

Wu, S., Kuhn, G., Diekmann, B., Lembke-Jene, L., Tiedemann, R., Zheng, X., et al. (2019). Surface sediment characteristics related to provenance and ocean circulation in the Drake Passage sector of the Southern Ocean. *Deep Sea Research Part I: Oceanographic Research Papers*, *154*, 103135. https://doi.org/10.1016/j.dsr.2019.103135

Wu, S., Lembke-Jene, L., Lamy, F., Arz, H. W., Nowaczyk, N., Xiao, W., et al. (2021). Orbital- and millennial-scale Antarctic Circumpolar Current variability in Drake Passage over the past 140,000 years. *Nature Communications*, *12*(1), 3948. https://doi.org/10.1038/s41467-021-24264-9

Yamazaki, K., Aoki, S., Katsumata, K., Hirano, D., & Nakayama, Y. (2021). Multidecadal poleward shift of the Southern Boundary of the Antarctic Circumpolar Current off East Antarctica. *Science Advances*, *7*(24), eabf8755. https://doi.org/10.1126/sciadv.abf8755